

# Advancing quantum imaging through learning theory

Yunkai Wang,<sup>1,2,3,\*</sup> Changhun Oh,<sup>4</sup> Junyu Liu,<sup>5,6</sup> Liang Jiang,<sup>6,†</sup> and Sisi Zhou<sup>1,7,3,‡</sup>

<sup>1</sup>*Perimeter Institute for Theoretical Physics, Waterloo, Ontario N2L 2Y5, Canada.*

<sup>2</sup>*Department of Applied Mathematics, University of Waterloo, Ontario N2L 3G1, Canada.*

<sup>3</sup>*Institute for Quantum Computing, University of Waterloo, Ontario N2L 3G1, Canada.*

<sup>4</sup>*Department of Physics, Korea Advanced Institute of Science and Technology, Daejeon 34141, Republic of Korea.*

<sup>5</sup>*Department of Computer Science, The University of Pittsburgh, Pittsburgh, PA 15260, USA.*

<sup>6</sup>*Pritzker School of Molecular Engineering, The University of Chicago, Chicago, IL 60637, USA.*

<sup>7</sup>*Department of Physics and Astronomy, University of Waterloo, Ontario N2L 3G1, Canada.*

We quantify performance of quantum imaging by modeling it as a learning task and calculating the Resolvable Expressive Capacity (REC). Compared to the traditionally applied Fisher information matrix approach, REC provides a single-parameter interpretation of overall imaging quality for specific measurements that applies in the regime of finite samples. We first examine imaging performance for two-point sources and generally distributed sources, referred to as compact sources, both of which have intensity distributions confined within the Rayleigh limit of the imaging system. Our findings indicate that REC increases stepwise as the sample number reaches certain thresholds, which are dependent on the source's size. Notably, these thresholds differ between direct imaging and superresolution measurements (e.g., spatial-mode demultiplexing (SPADE) measurement in the case of Gaussian point spread functions (PSF)). REC also enables the extension of our analysis to more general scenarios involving multiple compact sources, beyond the previously studied scenarios. For closely spaced compact sources with Gaussian PSFs, our newly introduced orthogonalized SPADE method outperforms the naively separate SPADE method, as quantified by REC.

*Introduction.*— Imaging quality using a single lens is influenced by several factors, including lens resolution, measurement design in the imaging plane, and sample number. Notably, it has been shown that by optimizing the measurement design, one can resolve two-point sources within the Rayleigh limit, surpassing the Rayleigh's criterion, as demonstrated through the calculation of Fisher Information [1]. This concept of quantum-metrology-inspired superresolution has since been expanded in various directions [2], including the imaging of general sources within the Rayleigh limit [3–5], as well as sources beyond the weak-source limit [6–8]. Additionally, there has been progress in imaging point sources in two and three dimensions [9–11]. These theories are experimentally demonstrated by various groups [12–17]. Quantum-metrology-inspired superresolution often uses Fisher information to bound estimation variance, but this approach has limitations. Imaging typically involves multiple parameters, requiring a Fisher information matrix, but optimal estimation is rarely achievable [18–20]. The need for a weight matrix introduces ambiguity. Furthermore, the asymptotic nature of Fisher information makes the threshold of number of samples to achieve the predicted accuracy unclear [21–23].

In this work, we approach imaging as a learning task. By treating a physical system as an input-output map, where the input consists of certain properties of the system,  $\theta$ , and the output corresponds to the measured de-

grees of freedom,  $\eta_j(\theta)$ , the learning task is to approximate a function,  $f(\theta)$ , using these measured degrees of freedom [24–36]. Naturally, due to sampling noise, we can only obtain an approximate estimation,  $\bar{\eta}_j(\theta)$ . Recently, a framework has been developed to analyze the resolvable function space for a general physical system in the presence of sampling noise [33, 37]. This framework introduces the concept of resolvable expressive capacity (REC),

$$C[f] = 1 - \min_w \frac{\mathbb{E}_\theta \left[ \mathbb{E}_\mathcal{X} \left[ \left( \sum_j W_j \bar{\eta}_j(\theta) - f(\theta) \right)^2 \right] \right]}{\mathbb{E}_\theta [f(\theta)^2]}, \quad (1)$$

where we take the expectation value for the output sample  $\mathcal{X}$  and the prior distribution  $p(\theta)$ ,  $f(\theta)$  is approximated by a linear combination of measured functions  $\sum_j W_j \bar{\eta}_j(\theta)$ . REC  $C[f]$  can be understood as the normalized mean-squared accuracy of approximating  $f(\theta)$ . In the case of quantum system, we can choose  $\eta_j(\theta)$  as the probability  $P_j$  of getting the  $j$ th measurement outcome in the POVM.

This approach addresses the two issues related to Fisher information mentioned earlier. The total REC,  $C_T = \sum_{l=0}^{\infty} C[f_l]$ , where  $\{f_l\}_l$  represents a complete and orthonormal set of basis functions, serves as a single-parameter quantification of imaging quality with a well-motivated interpretation: the total number of linearly independent functions  $f(\theta)$  that can be expressed as a linear combination of  $\bar{\eta}_j(\theta)$ . Moreover, this formalism provides a method to determine the threshold for the number of samples required. A more detailed introduction to this formalism, proposed in Ref. [37], is provided in Sec. A 2 of the Supplemental Information. Interestingly, within the Rayleigh limit, the total REC demon-

\* ywang10@perimeterinstitute.ca

† liangjiang@uchicago.edu

‡ szhou1@perimeterinstitute.ca

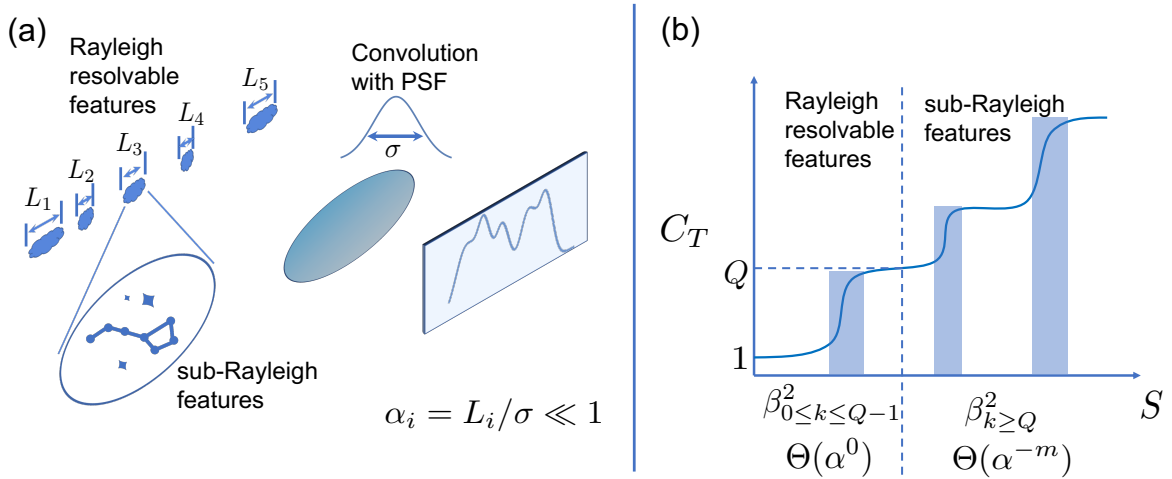


FIG. 1. Imaging of both Rayleigh resolvable features and sub-Rayleigh features. (a) Multiple compact sources of size  $L_i$  are imaged by a lens with a PSF width of  $\sigma$ . Besides Rayleigh-resolvable features, we would also like to extract information from sub-Rayleigh features, which are associated with the small parameter  $\alpha = L/\sigma$ . (b) The total REC,  $C_T$ , which shows a stepwise increase, is plotted as a function of the number of samples,  $S$ . The threshold of  $S$  for each stepwise increase of  $C_T$  in the shaded region is determined by the eigenvalue  $\beta_k^2$  associated with the corresponding eigentask in learning. Each time  $C_T$  increases by 1, there is a corresponding eigenvalue  $\beta_k^2$ , with the sample number threshold following  $S \sim \Theta(\beta_k^2)$ . The intensity of each compact source corresponds to resolvable features, which can be imaged with a constant number of samples, scaling as  $S \sim \beta_{0 \leq k \leq Q-1} = \Theta(\alpha^0)$ , independent of the source size. In contrast, sub-Rayleigh features that reveal detailed information about each compact source require a number of samples scaling inversely with the source size, following  $S \sim \beta_{k \geq Q} = \Theta(\alpha^{-m})$ , where  $\alpha$  is determined by the compact sources, and  $m$  depends on the order of moments.

strates a distinct stepwise increase. The advantage of superresolution becomes evident when comparing the different thresholds of this increase between direct imaging and superresolution.

Besides adopting a quantum learning perspective to study the imaging problem, we extend the existing discussions on superresolution [1–11] to encompass the broader challenge of imaging multiple compact sources, or equivalently, multiple clusters of sources, each constrained within the Rayleigh limit. A straightforward application of superresolution to individual compact sources, referred to as the *separate SPADE method*, fails to offer an advantage over direct imaging. This is because nearby sources, when spaced at distances not much greater than the width of the point spread function (PSF), introduce additional noise into the measurement. However, our generalized approach to superresolution, referred to as the *orthogonalized SPADE method*, can outperform both direct imaging and the separate superresolution method for nearby sources. As shown in Fig. 1, under this more generalized superresolution setting, the images exhibit two types of features: Rayleigh resolvable features and sub-Rayleigh features. The Rayleigh resolvable features correspond to the intensity of each compact source, which can be measured with a constant number of samples independent of the source size for both direct imaging and superresolution methods. In contrast, the sub-Rayleigh features involve details below the Rayleigh limit, requiring the number of samples to scale inversely

with the source size, where carefully designed superresolution methods demonstrate clear advantages. This discussion advances the superresolution to a more practical scenario, where the focus shifts from a single compact source within the Rayleigh limit to multiple compact sources.

*Resolving two-point sources.*—As a simplest example, we begin with the imaging of two incoherent point sources in one dimension. A single photon received on the image plane can be described as  $\rho(L) = \frac{1}{2}(|\psi_1\rangle\langle\psi_1| + |\psi_2\rangle\langle\psi_2|)$ , where  $|\psi_i\rangle = \int du \psi(u - u_i)|u\rangle$ ,  $|u\rangle = a_u^\dagger|0\rangle$  is the single photon state at position  $u$ , and we choose the PSF  $\psi(u) = \exp(-u^2/4\sigma^2)/(2\pi\sigma^2)^{1/4}$ . Define the separation  $L$ , which is the input of learning task  $\theta = L$  and assume  $u_2 = L/2$ ,  $u_1 = -L/2$ . To enable analytical analysis, we focus on the binary SPADE measurement, which is capable of achieving superresolution in resolving two-point sources as introduced in Ref. [1], where  $M_0 = |\phi_0\rangle\langle\phi_0|$ ,  $M_1 = I - M_0$ ,  $|\phi_0\rangle = \int du \phi_0(u)|u\rangle$ ,  $\phi_0(u) = \frac{1}{(2\pi\xi^2)^{1/4}} \exp(-\frac{u}{4\xi^2})$ , and  $\xi$  is a parameter left to be determined. Assuming the prior knowledge about the separation is described as  $p(L) = \frac{1}{\sqrt{2\pi}\gamma} \exp(-\frac{L^2}{2\gamma^2})$ , we can calculate the total REC,  $C_T$ , which here represents the total number of linearly independent functions  $f(L)$  that can be expressed as a linear combination of the measured probabilities  $P_k = \text{tr}(\rho(L)M_k)$ , using the formalism derived in Ref. [37] and reviewed in Sec. A 2

of Supplemental,

$$C_T = \sum_{k=0}^{K-1} \frac{1}{1 + \beta_k^2/S}, \quad (2)$$

$$D_{kj} = \delta_{kj} \text{Tr} \left\{ M_k \hat{\rho}^{(1)} \right\}, \quad G_{jk} = \text{Tr} \left\{ (M_j \otimes M_k) \hat{\rho}^{(2)} \right\}, \quad (3)$$

$$\hat{\rho}^{(t)} = \int \rho(L)^{\otimes t} p(L) dL, \quad (4)$$

$$V = D - G, \quad Vr_k = \beta_k^2 Gr_k, \quad (5)$$

where  $S$  is the number of samples,  $\beta_k^2$  and  $r_k$  are the  $k$ th eigenvalue and eigenvector (in increasing order), satisfying the orthonormal condition  $r_k^\dagger Gr_j = \delta_{kj}$  from the generalized eigenvalue problem. The eigenbasis  $r_k$  correspond to a minimal and complete set of resolvable functions  $\sum_m r_{km} P_m$  that saturate the available REC of the system (see details in Sec. A 2 of Supplemental). Here,  $P_m$  denotes the probability of obtaining the  $m$ th outcome in the POVM. More calculation details can be found in Sec. B of Supplemental. Assuming  $\gamma \ll \sigma, \xi$ , we find that the smallest value of  $\beta_k^2$  occurs when choosing  $\xi = \sigma$ ,

$$\begin{aligned} \beta_0^2 &= 0, \\ \beta_1^2 &= \frac{8}{\alpha^2} + \frac{3}{4} - \frac{1}{64} \alpha^2 + O(\alpha^4), \quad \alpha = \gamma/\sigma, \end{aligned} \quad (6)$$

where  $\alpha$  is roughly the ratio between the separation and width of the PSF and  $\alpha \ll 1$  when the two-point sources are very close to each others.

We can compare this with the direct imaging case, where we directly project onto each spatial mode  $E_x = |x\rangle \langle x|_x$ . In this case, we numerically calculate that  $\beta_0^2 = O(1)$ ,  $\beta_1^2 = \Theta(\alpha^{-4})$ , and  $\beta_2^2 = \Theta(\alpha^{-8})$  after discretizing the spatial coordinate, with more details provided in Sec. B and Sec. F of the Supplemental Information. The much larger eigenvalue  $\beta_1^2$  in direct imaging indicates poorer performance compared to binary SPADE, as it requires a larger number of samples  $S$  to achieve the same  $C_T$ .

*Resolving compact sources.*—We consider the problem of imaging a generally distributed source with a spatially bounded size significantly below the Rayleigh limit, referred to as a *compact source* in this Letter. Assume the normalized source intensity  $I(u)$  is confined within the interval  $[-L/2, L/2]$ . We can define the moments as  $\int du I(u) \left(\frac{u-u_0}{L}\right)^n = x_n$ , which completely describe the source and are the input for the learning task  $\theta = \vec{x} = [x_0, x_1, x_2, \dots]$ . Within the Rayleigh limit,  $\alpha = L/\sigma \ll 1$ , where  $\sigma$  represents the width of the PSF, the size of the compact source is significantly smaller than the resolution limit. We present an intuitive argument based on characteristic polynomials in Sec. C 1 of the Supplemental for the direct imaging

$$\beta_0^2 = 0, \quad \beta_1^2 = \Theta(\alpha^{-2}), \quad \beta_2^2 = \Theta(\alpha^{-4}), \quad \dots \quad (7)$$

where  $\beta_0^2 = 0$  is a trivial eigenvalue which corresponds to the fact that  $\sum_m P_m = 1$ . Furthermore, a rigorous analytical proof, based on perturbation theory, is carried out

to show  $\beta_0^2 = 0$ ,  $\beta_1^2 = \Theta(\alpha^{-2})$ ,  $\beta_{k \geq 2}^2 = \omega(\alpha^{-2})$  for any prior  $p(\vec{x})$ . The scalings of the first four eigenvalues are also confirmed by the numerical calculations presented below for a prior generated randomly. We expect the scalings of eigenvalues  $\beta_k^2 = \Theta(\alpha^{-2k})$  to hold for eigenvalues with higher indices with any prior  $p(\vec{x})$ . Note that prior knowledge can influence the prefactor of each  $\beta_k^2$ , and consequently, the threshold of  $C_T$  will also include a prefactor independent of  $\alpha$ , determined by  $p(\vec{x})$ . The effects of these eigenvalue prefactors will be discussed further below. The eigenbasis corresponds to  $\sum_m r_{nm} P_m$  as a function of  $\vec{x}$ , representing the eigentasks, whose REC is  $1/(1 + \beta_k^2/S)$ . Our goal is to approximate each moment  $x_n$  using a linear combination of  $P_m$ . Here,  $x_n$  serves as both the input and the target function we aim to approximate. Note that the functions  $\sum_m r_{nm} P_m$  given by the eigenbasis in general are not approximations of the moments. However, for direct imaging of one compact source, we observe that they converge to  $x_n$  in the limit of small  $\alpha$ . As detailed in in Sec. C 1 and Sec. C 3 of the Supplemental, the first eigenvector  $r_0 \propto [1, 1, \dots, 1]^T$ , providing an approximation for  $x_0 = \int du I(u) = 1$ , which is trivial. The second eigenvector,  $r_1$  where the  $\Theta(1)$  term in  $\sum_m r_{1m} P_m$  is cancelled out, is dominated by terms proportional to  $x_1 \alpha$  as  $\alpha \rightarrow 0$ . Similarly, the eigenvector  $r_n$  provides an appropriate linear combination of  $P_k$ , yielding a good approximation for  $x_n$ .

For superresolution, we adopt the construction of measurement from Ref. [5] reviewed in Sec. A 1 of Supplemental. The measurement scheme from Ref. [5] works universally for any PSF. But for the Gaussian PSF, this measurement aligns with the SPADE measurement introduced in Ref. [1] with slight difference as clarified in Sec. A 1 of Supplemental. For simplicity, we still refer to this as the SPADE method here and throughout the discussion, but all the analytical results presented below apply to any PSF and to the measurement approach from Ref. [5]. In the Sec. C 2 of Supplemental, we present an intuitive argument based on characteristic polynomials for the SPADE method

$$\begin{aligned} \beta_0^2 &= 0, \quad \beta_1^2 = \Theta(\alpha^{-2}), \quad \beta_2^2 = \Theta(\alpha^{-2}), \\ \beta_3^2 &= \Theta(\alpha^{-4}), \quad \beta_4^2 = \Theta(\alpha^{-4}), \quad \dots \end{aligned} \quad (8)$$

Compared to direct imaging, the SPADE method achieves smaller  $\beta_k^2$ , which significantly reduces the required  $S$  to achieve the same  $C_T$ . Furthermore, a rigorous proof based on perturbation theory calculation shows  $\beta_0^2 = 0$ ,  $\beta_1^2 = \Theta(\alpha^{-2})$ ,  $\beta_2^2 = \Theta(\alpha^{-2})$ ,  $\beta_{k \geq 3}^2 = \omega(\alpha^{-2})$  for any prior  $p(\vec{x})$ . And the scaling of the first five eigenvalues are confirmed by the numerical calculations presented below for a randomly generated prior. We believe that the rule  $\beta_k^2 = \Theta(\alpha^{2\lceil k/2 \rceil})$  holds for eigenvalues with higher indices. As reviewed in Sec. A 1 of the Supplemental, the first two leading orders of each probability distribution for the SPADE method is proportional to  $x_{2n} \alpha^{2n}$  and  $x_{2n+1} \alpha^{2n+1}$ , their linear combination provides a good approximation of  $x_{2n}$  and  $x_{2n+1}$  and the

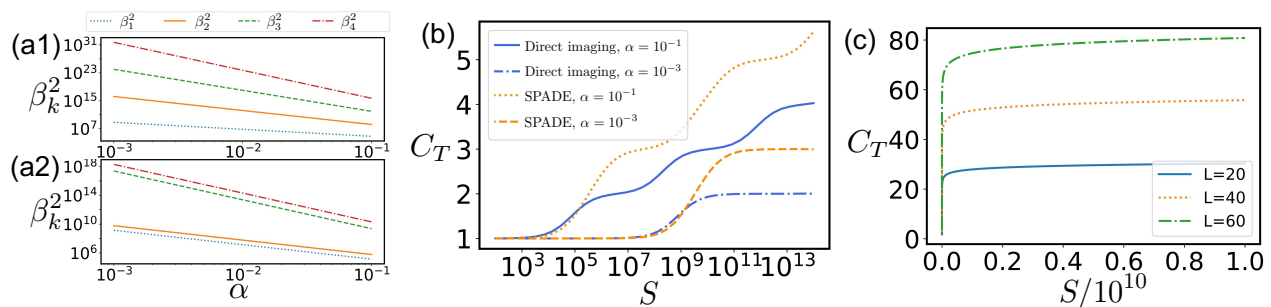


FIG. 2. (a1)-(a2) Scaling of the  $\beta_k^2$  as a function of  $\alpha$  for (a1) direct imaging and (a2) SPADE method, when imaging a generally distributed compact source.  $\beta_0^2 = 0$  is omitted from the plot. Note that  $\beta_{3,4}^2$  in Fig. 2(a1) is interpolated using values calculated for cases where  $\alpha > 10^{-1}$  that are not explicitly shown in the plot. (b) Total REC  $C_T$  for direct imaging and the SPADE method as a function of  $S$ , when imaging one generally distributed compact source with different  $\alpha$ . (c) Total REC for direct imaging as a function of  $S$  for a general source with size  $L = 20, 40, 60$  respectively and width of PSF  $\sigma = 1$ .

coefficients in the linear combination are determined by the eigenvectors. Again,  $\beta_0^2$  trivially confirms the normalization of the probability, while  $\beta_{2k+1}$  and  $\beta_{2k+2}$  quantify the accuracy of approximating  $x_{2k+1}$  and  $x_{2k}$ . Note that, compared to the direct imaging case, the estimation of  $x_1$  demonstrates similar performance, while the advantage of superresolution becomes apparent starting from  $x_2$ , consistent with the observation in Ref. [5].

We numerically confirm the scaling behavior described in Eqs. 7 and 8, as shown in Fig. 2(a). For these calculations, we select the PSF as  $\psi(u) = \exp(-u^2/4\sigma^2)/(2\pi\sigma^2)^{1/4}$ . All numerical calculations in this work assume a Gaussian PSF; however, our method is applicable to any PSF, with the Gaussian PSF as a specific example. We choose a prior distribution for the moments  $\vec{x}$  by randomly generating a set of images and assuming that these images appear with equal probability, thereby establishing a prior distribution  $p(\vec{x})$ , as detailed in Sec. F of the Supplemental. For illustration purpose, we plot the data for only one instance of the randomly generated prior distributions in Fig. 2(a) (and in all figures below where the prior is picked randomly). However, we expect that the scaling of  $\beta_k^2$  and the stepwise increase behavior of  $C_T$  hold for any prior information, as consistently observed by comparing multiple randomly generated prior distributions. Additional examples with different priors are presented in Sec. F of the Supplemental. Values exceeding approximately  $10^{15}$  in Fig. 2(a) have been interpolated using a straight-line fit based on the data at larger  $\alpha$  to mitigate precision loss in the numerical calculations. We perform this straight-line interpolation for all  $\beta_k^2$ - $\alpha$  plots in this work. Fig. 2(a) illustrates that, the superresolution case has pairs of eigenvalues  $\{\beta_{2k-1}^2, \beta_{2k}^2\}_{k \geq 1}$  with the same scaling starting from  $k = 1$ , consistent with our analytical proof. We also demonstrate the significance of  $\beta_k^2$  as the threshold for the stepwise increase in the total REC  $C_T$ , as shown in Fig. 2(b). For direct imaging,  $C_T$  increases by 1 at each step, while for the SPADE method,  $C_T$  increases by 2 per step, as expected. As  $\alpha$  decreases, the

plateau regions expand. Note that the threshold of  $S$  is not precisely located at  $\alpha^{-2n}$  in each case. This deviation arises from a constant prefactor in  $\beta_k^2$ . This constant prefactor is independent of  $\alpha$  and is approximately  $10^2$  in Fig. 2(b). This is reasonable because, even in the simpler imaging task where sources are extended outside the Rayleigh limit (i.e.,  $\alpha \gg 1$ ), hundreds or more samples are still required to effectively image a source. Additionally, we numerically confirm in Sec. C3 of the Supplemental that the first five eigenvectors converge to the zeroth-order approximation from the perturbation theory as  $\alpha \rightarrow 0$ . So far, our discussion has focused on sources where the entire source lies within the Rayleigh limit. In this case, the total intensity, trivially equal to 1, is the Rayleigh resolvable feature that contributes to the total REC when only a constant number of samples (smaller than  $1/\alpha^2$ ) is available. The separation  $L$  and the moments  $\vec{x}$ , however, are considered sub-Rayleigh features that contribute to the total REC when  $\Omega(\alpha^{-2})$  samples are available. As we will see later, the Rayleigh resolvable features can become nontrivial when dealing with multiple compact sources.

*Direct imaging of general sources beyond the Rayleigh limit.*—A natural question is what the total REC would be for a general imaging task using direct imaging and how to interpret its meaning. Intuitively, when imaging a source of size  $L$  with a lens where the PSF has a width  $\sigma$ , the resulting image is a blurred version of the original, with the blur size being  $\sigma$ . The total REC represents the number of degrees of freedom we can extract from the measurement, and since the image is blurred, this is roughly upper bounded by  $L/\sigma$ . To confirm this, we perform a numerical calculation and plot the total REC as a function of sample number  $S$  for different values of  $L$ , as shown in Fig. 2(c). As expected, the total  $C_T$  soon reaches a (slowly increasing) plateau as  $S \rightarrow \infty$ . We randomly generate a set of images and establish a random prior distribution for the intensity at each pixel for Fig. 2(c). Sec. D of the Supplemental provides additional numerical details and includes a plot showing that, as the

source size  $L$  increases, the total  $C_T$  grows approximately linearly.

*New superresolution methods on multiple compact sources.*—We now want to consider the scenario where we have multiple compact sources, each with a size within the Rayleigh limit, but collectively distributed over a region larger than the Rayleigh limit. The quantum state from these multiple compact sources is given by

$$\rho = \sum_{q=1}^Q \int dud u_1 du_2 I_q(u) \psi(u - u_1) |u_1\rangle \langle u_2| \psi^*(u - u_2), \quad (9)$$

where  $Q$  is the number of compact sources,  $I_q(u)$  is the intensity distribution for  $q$ th compact source. We can expand near the centroid  $u_q$  of  $q$ th source and reorganize the state as

$$\begin{aligned} \rho &= \sum_{q=1}^Q \sum_{m,n=0}^{\infty} x_{m+n,q} \left| \psi_q^{(m)} \right\rangle \left\langle \psi_q^{(n)} \right|, \\ \left| \psi_q^{(m)} \right\rangle &= \int du \psi_q^{(m)}(u) |u\rangle, \\ \psi_q^{(n)}(v) &= \frac{\partial^n \psi(v - u)}{\partial u^n} \Big|_{u=u_q} \frac{L_q^n}{n!}, \end{aligned} \quad (10)$$

where  $L_q$  is the size (diameter) of  $q$ th source,  $x_{n,q} = \int du I_q(u) \left( \frac{u - u_q}{L_q} \right)^n$  is the  $n$ th moment for the  $q$ th source and are the input for the learning task  $\theta = [x_{0,1}, x_{1,1}, x_{2,1}, \dots, x_{0,Q}, x_{1,Q}, x_{2,Q}, \dots]$ . In Sec. E1 of the Supplemental, we present an intuitive argument based on the characteristic polynomial in direct imaging,

$$\begin{aligned} \beta_0^2 &= 0, \quad \beta_{1 \leq i \leq Q-1}^2 = \Theta(1), \\ \beta_{Q \leq i \leq 2Q-1}^2 &= \Theta(\alpha^{-2}), \quad \beta_{2Q \leq i \leq 3Q-1}^2 = \Theta(\alpha^{-4}), \dots \end{aligned} \quad (11)$$

where  $\alpha_q = \max L_q / \sigma$ . Here, we assume that  $L_q$  does not differ significantly, allowing the different  $L_q$  values to be incorporated into the constant coefficients. The scaling is numerically confirmed in Fig. 3 as detailed below for the first six eigenvalues with a randomly generated prior, and we expect  $\beta_k^2 = \Theta(\alpha^{2\lceil k/Q \rceil})$  to hold for eigenvalues with higher indices with any prior  $p(\vec{x})$ .

To improve imaging performance, one could apply the SPADE method to each compact source individually—a technique referred to here as the *separate SPADE method*. Unfortunately, it only achieves the same scaling as direct imaging when the sources are not sufficiently spaced apart. This is because the proximity of other compact sources introduces significant noise when estimating higher-order moments, as detailed in Sec. E2. Alternatively, we can construct the orthonormal basis  $|b_j^{(l)}\rangle$  using the Gram-Schmidt procedure, such that

$$\left\langle \psi_k^{(m)} \middle| b_j^{(l)} \right\rangle \begin{cases} = 0 & m \leq l - 1 \\ = 0 & m = l \text{ \& } k \leq j - 1 \\ \neq 0 & \text{otherwise} \end{cases} \quad (12)$$

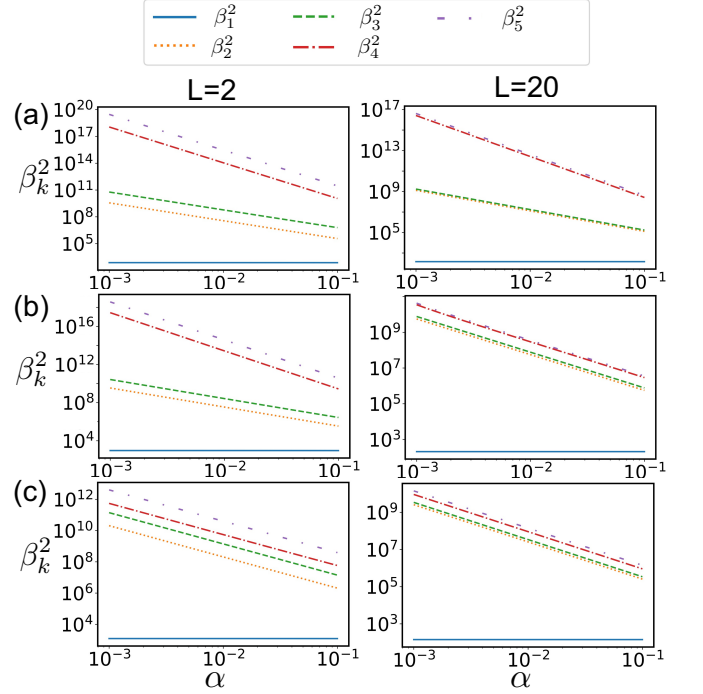


FIG. 3. Scaling of the  $\beta_k^2$  as a function of  $\alpha$  for imaging two compact sources with distance  $L/2$ . We consider three different cases: (a) direct imaging (b) separate SPADE method (c) orthogonalized SPADE method. Width of PSF  $\sigma = 1$ .

Choose POVM as the projection onto

$$\left| \phi_{j\pm}^{(l)} \right\rangle = \frac{1}{\sqrt{2}} \left( \left| b_j^{(l)} \right\rangle \pm \left| b_j^{(l+1)} \right\rangle \right), \quad (13)$$

where  $j = 1, 2, 3, \dots, Q$ ,  $l = 0, 1, 2, \dots, \infty$ . The key intuition behind this construction is to ensure that when estimating the  $x_{n,q}$  term in the  $\Theta(\alpha^n)$  order, lower-order terms must vanish in the probability distribution, particularly those contributions from nearby compact sources. We refer to this new approach as the *orthogonalized SPADE method*, as it projects onto a basis that is an orthogonalization of the separate SPADE method. This construction applies analogously to any PSF beyond Gaussian PSF. Note that for a single compact source, the separate SPADE and orthogonalized SPADE methods are identical, both referred to as the SPADE method. In Sec. E3 of the Supplemental Material, we present an intuitive argument based on characteristic polynomials for orthogonalized SPADE method,

$$\begin{aligned} \beta_0^2 &= 0, \quad \beta_{1 \leq i \leq Q-1}^2 = \Theta(1), \\ \beta_{Q \leq i \leq 3Q-1}^2 &= \Theta(\alpha^{-2}), \quad \beta_{3Q \leq i \leq 5Q-1}^2 = \Theta(\alpha^{-4}), \dots \end{aligned} \quad (14)$$

The scaling is numerically confirmed in Fig. 3 as detailed below for the first six eigenvalues with a randomly generated prior, and we expect  $\beta_k^2 = \Theta(\alpha^{2\lceil k/Q \rceil})$  to hold for eigenvalues with higher indices with any prior  $p(\vec{x})$ . It is then clear that there are  $Q$  Rayleigh resolvable features

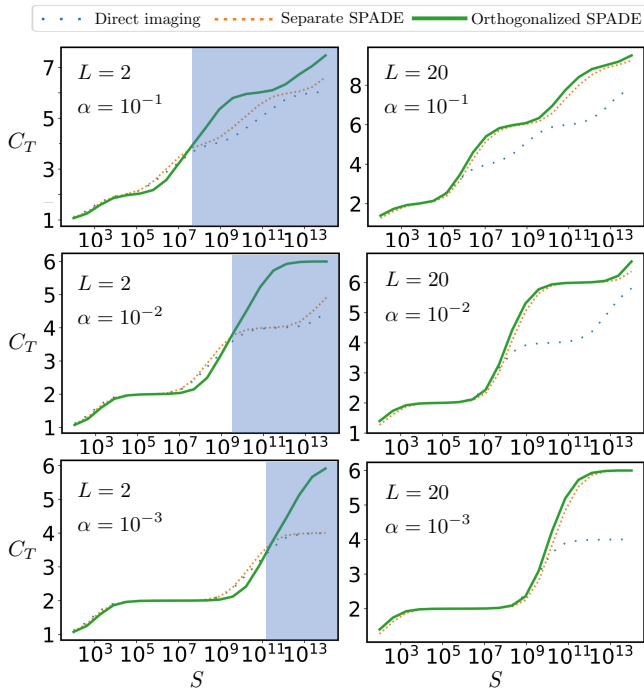


FIG. 4. Total REC  $C_T$  for direct imaging, the separate SPADE method and the orthogonalized SPADE method as a function of  $S$  for imaging of two compact sources with  $\alpha = 10^{-1}, 10^{-2}, 10^{-3}$ , number of compact source  $Q = 2$ ,  $\sigma = 1$ . The distance between the centroid of the two compact sources is  $L/2$ . When  $L = 2$ , the orthogonalized SPADE method demonstrates a clear advantage over both the separate SPADE method and direct imaging in the shaded region. When  $L = 20$ , the performance of SPADE and orthogonalized SPADE is comparable (essentially because they become equivalent when the two compact sources are sufficiently far apart) and both outperform direct imaging. Overall, the orthogonalized SPADE protocol demonstrates excellent performance, achieving a high  $C_T$  (compared to the best from direct and SPADE protocols) for various choices of  $L = 2$  and  $L = 20$ , as well as across a wide range of sample sizes  $S$ .

corresponding to the intensity of each compact sources, and the number of sub-Rayleigh features also increases by a factor of  $Q$ .

We perform a numerical analysis of the scaling behavior for three different methods. Assume two compact sources with centroids at  $-L/4$  and  $L/4$ , with a random prior distribution for the moments (by randomly generating a set of images). As shown in Fig. 3, we considered (a) direct imaging, (b) separate SPADE method, and (c) orthogonalized SPADE method. When the sources are well separated ( $L \gg \sigma$ ), both separate SPADE and orthogonalized SPADE achieve the expected scaling, with four  $\beta_k^2$  terms scale as  $\Theta(\alpha^{-2})$ , compared to two for direct imaging. The doubling in the number of eigenvalues with the scaling  $\Theta(\alpha^{-2n})$  for each  $n$  aligns with expectations for two compact sources. However, when the sources are closer ( $L = 2$ ,  $\sigma = 1$ ), performance of separate SPADE

method is strongly degraded, reducing the scaling to that of direct imaging, with only two  $\beta_k^2$  terms at  $\Theta(\alpha^{-2})$ . In contrast, our orthogonalized SPADE method still maintains four  $\beta_k^2$  terms at  $\Theta(\alpha^{-2})$ .

In Fig. 4, we demonstrate the role of  $\beta_k^2$  as the thresholds for stepwise increases in total REC  $C_T$  for two compact sources. When  $L = 2$  (sources close together), direct imaging and separate SPADE show that  $C_T$  increases by 2 at each step after the initial two  $\Theta(1)$  eigenvalues. In contrast, for orthogonalized SPADE,  $C_T$  is increased by 4 after the initial two  $\Theta(1)$  eigenvalues, highlighting the advantage of our method for two close compact sources. When  $L = 20$  (with sources well separated), both separate SPADE and orthogonalized SPADE yield a  $C_T$  increase of 4 at each step. Note that in certain regions of the sample number when  $\alpha = 10^{-2}$ , the orthogonalized SPADE method may perform slightly worse than the separate SPADE method. This difference arises from the different constant prefactors in  $\beta_k^2$ . To ensure optimal performance, we can adopt an adaptive approach: for a given sample size, we select either the orthogonalized or separate SPADE method based on the total REC of each method, choosing the one that offers superior performance.

In Fig. 5, we numerically illustrate the shape of the constructed basis for the separate SPADE method and the orthogonalized SPADE method, considering different distances between the centroids of the two compact sources. It is evident that when the two compact sources are close to each other, the basis for the separate and orthogonalized SPADE methods differ significantly. However, when the two compact sources are sufficiently far from each other, the basis for the separate and orthogonalized SPADE methods become nearly identical. Given the complicated form of the basis, the spatial light modulator could serve as a practical tool for its implementation, as previously discussed in the context of superresolution [38]. We also demonstrate in Sec. E4 of the Supplemental that the Hermite-Gaussian mode sorter [39–43] can be used to implement the orthogonalized SPADE method with some additional steps for Gaussian PSF.

An intriguing question is whether, when a general source cannot be split into multiple compact sources, we can still split the source into  $Q$  small pieces and apply our orthogonalized SPADE method, improving the imaging performance. We previously discussed that direct imaging of a general source extended outside the Rayleigh limit has an upper bound on total REC  $C_T$ , roughly determined by  $L/\sigma$ . A similar limitation applies to orthogonalized SPADE method. Each source generates a set of states  $\{|\psi_q^{(m)}\rangle\}_{m=0,1,2,\dots}$ , which are used to construct  $|b_j^{(l)}\rangle$  via the Gram-Schmidt procedure. When  $Q \gg L/\sigma$ , the differences between  $|\psi_q^{(m)}\rangle$  for different  $q$  can be vanishingly small, leading to the potentially suboptimal performance of orthogonalized SPADE method due to large prefactors of the eigenvalues  $\beta_k^2$ . In Sec. E3 of the Sup-

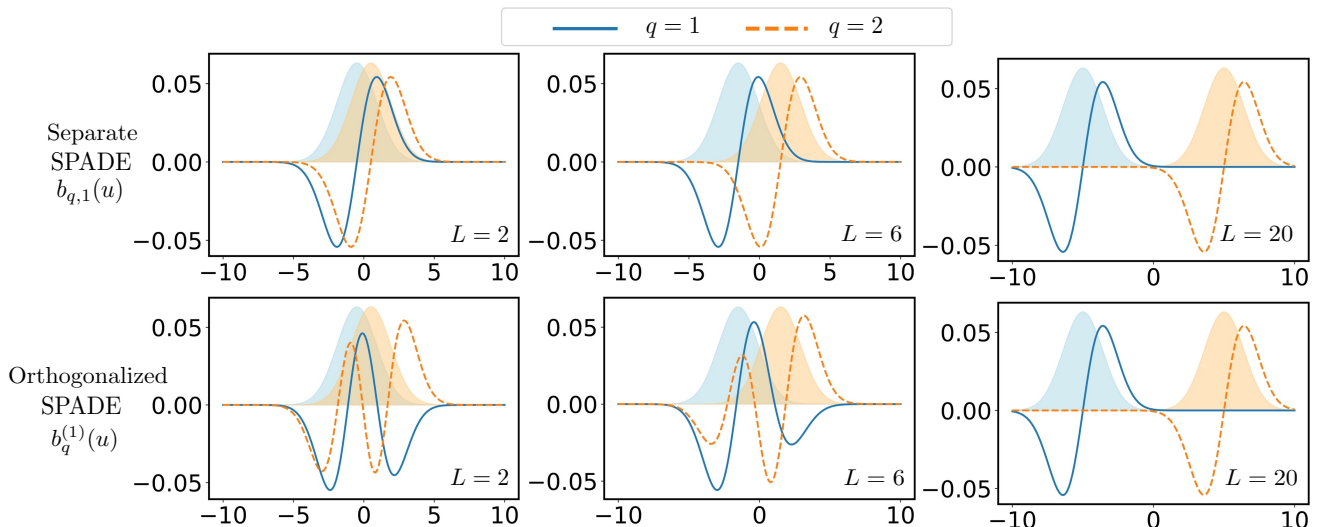


FIG. 5. We compare the basis states constructed in Eq. 12 for the orthogonalized SPADE measurement,  $|b_q^{(l=1)}\rangle = \int du b_q^{(1)}(u) |u\rangle$ , with the corresponding basis states for the separate SPADE measurement,  $|b_{q,1}\rangle = \int du b_{q,1}(u) |u\rangle$ . Here,  $q = 1, 2$  corresponds to the scenario of two compact sources ( $Q = 2$ ) with centroids located at  $\pm L/4$ . We examine cases where  $L = 2, 6, 20$ . The shaded regions show two Gaussian PSFs of width  $\sigma = 1$  located at the centers of two compact sources, that are used to construct the basis states  $|b_q^{(l)}\rangle$  and  $|b_{q,m}\rangle$ .

plemental, we demonstrate that when  $Q$  exceeds roughly  $L/\sigma$ , the stepwise increase in  $C_T$  is smoothed out, and numerically, we find that both the separate SPADE and the orthogonalized SPADE no longer offer advantages over direct imaging. Furthermore, the previous discussion assumes each compact source has similar  $\alpha_q$  which can be incorporated into the constant coefficients, but in practice, each compact source may have different values of  $\alpha_q$ . As we also showed in Sec. E 3 of the Supplemental, variations in  $\alpha$  among the compact sources also smooth out the stepwise increase in  $C_T$ . Therefore, when imaging a general source without a compact structure, we expect  $C_T$  to behave similarly to what is shown in Fig. 2(c). In conclusion, the superresolution methods from Ref. [1, 5] can be properly generalized to resolve multiple compact sources but may fail for generally distributed sources.

*Conclusion.*—In this work, we apply learning theory to study imaging problems, quantifying imaging quality using REC, a single-parameter metric that also enables analysis in the regime of finite samples. We demonstrate that quantum-metrology-inspired superresolution exhibits a stepwise increase in total REC, with thresholds determined by the ratio of source size to PSF width. Additionally, we extend the superresolution method to multiple compact sources. While Fisher information calculations in Ref. [1, 5] highlight differences between superresolution and direct imaging, Fisher information alone does not ensure that these performance levels are achievable with a reasonable number of samples. Furthermore, to provide a clear single-parameter measure, a weight matrix for the Fisher information must be selected. It

might not be clear how to appropriately weight each moment to quantify overall imaging quality, a issue that are effectively addressed using REC.

Our results generalize the quantum-metrology-inspired superresolution method to treat compact sources centered at multiple locations, while previous superresolution studies mainly focused on single compact source. Still it remains to be investigated whether further generalizations could enhance its applicability to universal imaging tasks. It would also be worthwhile to investigate other potentially advantageous imaging protocols, e.g., entangled measurements on multiple copies of photon states, which exhibit advantages over separable measurements in tomography [44, 45]. We may also explore the potential applications of quantum computing schemes [46–48], where the quantum advantage inherent in these schemes could benefit specific imaging tasks.

*Acknowledgements.*—We would like to thank Hakan E. Tureci for helpful discussion. Y.W. and S.Z. acknowledges funding provided by Perimeter Institute for Theoretical Physics, a research institute supported in part by the Government of Canada through the Department of Innovation, Science and Economic Development Canada and by the Province of Ontario through the Ministry of Colleges and Universities. Y.W. also acknowledges funding from the Canada First Research Excellence Fund. L.J. acknowledges support from the the ARO(W911NF-23-1-0077), ARO MURI (W911NF-21-1-0325), AFOSR MURI (FA9550-19-1-0399, FA9550-21-1-0209, FA9550-23-1-0338), DARPA (HR0011-24-9-0359, HR0011-24-9-0361), NSF (OMA-1936118, ERC-1941583,

OMA-2137642, OSI-2326767, CCF-2312755), NTT Research, Packard Foundation (2020-71479), and the Marshall and Arlene Bennett Family Research Program. J.L. acknowledges startup funds provided by the Department of Computer Science, School of Computing and Information, the University of Pittsburgh, Pittsburgh Quantum Institute (PQI), funding from IBM Quantum through the Chicago Quantum Exchange, and AFOSR MURI (FA9550-21-1-0209). C.O. acknowledges support from Quantum Technology R&D Leading Program (Quantum Computing) (RS-2024-00431768) through the National Research Foundation of Korea (NRF) funded by the Korean government (Ministry of Science and ICT (MSIT))

*Author contributions* - Y.W. carried out the analytical calculation and the numerical simulation. L.J. conceived the project. S.Z., J.L., and L.J. supervised the project. All authors contributed to the development of ideas and the writing of the manuscript.

*Competing interests* - The authors declare no competing interests.

*Code availability* - All codes used to generate the figures in this paper are available with the arXiv posting of this paper as arXiv ancillary files.

*Correspondence* and requests for materials should be addressed to Yunkai Wang, Sisi Zhou or Liang Jiang.

- 
- [1] M. Tsang, R. Nair, and X.-M. Lu, Quantum theory of superresolution for two incoherent optical point sources, *Physical Review X* **6**, 031033 (2016).
- [2] S. Pirandola, B. R. Bardhan, T. Gehring, C. Weedbrook, and S. Lloyd, Advances in photonic quantum sensing, *Nature Photonics* **12**, 724 (2018).
- [3] M. Tsang, Quantum limit to subdiffraction incoherent optical imaging, *Physical Review A* **99**, 012305 (2019).
- [4] M. Tsang, Subdiffraction incoherent optical imaging via spatial-mode demultiplexing, *New Journal of Physics* **19**, 023054 (2017).
- [5] S. Zhou and L. Jiang, Modern description of rayleigh's criterion, *Physical Review A* **99**, 013808 (2019).
- [6] Y. Wang, Y. Zhang, and V. O. Lorenz, Superresolution in interferometric imaging of strong thermal sources, *Physical Review A* **104**, 022613 (2021).
- [7] R. Nair and M. Tsang, Far-field superresolution of thermal electromagnetic sources at the quantum limit, *Physical review letters* **117**, 190801 (2016).
- [8] C. Lupo and S. Pirandola, Ultimate precision bound of quantum and subwavelength imaging, *Physical review letters* **117**, 190802 (2016).
- [9] C. Napoli, S. Piano, R. Leach, G. Adesso, and T. Tufarelli, Towards superresolution surface metrology: quantum estimation of angular and axial separations, *Physical review letters* **122**, 140505 (2019).
- [10] Z. Yu and S. Prasad, Quantum limited superresolution of an incoherent source pair in three dimensions, *Physical review letters* **121**, 180504 (2018).
- [11] S. Z. Ang, R. Nair, and M. Tsang, Quantum limit for two-dimensional resolution of two incoherent optical point sources, *Physical Review A* **95**, 063847 (2017).
- [12] F. Yang, A. Tashchilina, E. S. Moiseev, C. Simon, and A. I. Lvovsky, Farfield linear optical superresolution via heterodyne detection in a higher-order local oscillator mode, *Optica* **3**, 1148 (2016).
- [13] Z. S. Tang, K. Durak, and A. Ling, Fault-tolerant and finite-error localization for point emitters within the diffraction limit, *Opt. Express* **24**, 22004 (2016).
- [14] M. Paúr, B. Stoklasa, Z. Hradil, L. L. Sánchez-Soto, and J. Rehacek, Achieving the ultimate optical resolution, *Optica* **3**, 1144 (2016).
- [15] W.-K. Tham, H. Ferretti, and A. M. Steinberg, Beating rayleigh's curse by imaging using phase information, *Phys. Rev. Lett.* **118**, 070801 (2017).
- [16] M. Parniak, S. Borówka, K. Boroszko, W. Wasilewski, K. Banaszek, and R. Demkowicz-Dobrzanski, Beating the rayleigh limit using two-photon interference, *Phys. Rev. Lett.* **121**, 250503 (2018).
- [17] U. Zanforlin, C. Lupo, P. W. Connolly, P. Kok, G. S. Buller, and Z. Huang, Optical quantum super-resolution imaging and hypothesis testing, *Nat. Commun.* **13**, 5373 (2022).
- [18] M. Szczykulska, T. Baumgratz, and A. Datta, Multiparameter quantum metrology, *Advances in Physics: X* **1**, 621 (2016).
- [19] S. Ragy, M. Jarzyna, and R. Demkowicz-Dobrzański, Compatibility in multiparameter quantum metrology, *Physical Review A* **94**, 052108 (2016).
- [20] J. Liu, H. Yuan, X.-M. Lu, and X. Wang, Quantum fisher information matrix and multiparameter estimation, *Journal of Physics A: Mathematical and Theoretical* **53**, 023001 (2020).
- [21] M. Hayashi, Two quantum analogues of fisher information from a large deviation viewpoint of quantum estimation, *Journal of Physics A: Mathematical and General* **35**, 7689 (2002).
- [22] V. Spokoiny, Parametric estimation. Finite sample theory, *The Annals of Statistics* **40**, 2877 (2012).
- [23] J. J. Meyer, S. Khatiri, D. S. França, J. Eisert, and P. Faist, Quantum metrology in the finite-sample regime, arXiv preprint arXiv:2307.06370 (2023).
- [24] S. Boyd and L. Chua, Fading memory and the problem of approximating nonlinear operators with volterra series, *IEEE Trans. Comput.-Aided Des. Integr. Circuits Syst.* **32**, 1150 (1985).
- [25] G. Tanaka, T. Yamane, J. B. Héroux, R. Nakane, N. Kanazawa, S. Takeda, H. Numata, D. Nakano, and A. Hirose, Recent advances in physical reservoir computing: A review, *Neural Netw.* **115**, 100 (2019).
- [26] P. Mujal, R. Martínez-Peña, J. Nokkala, J. García-Beni, G. L. Giorgi, M. C. Soriano, and R. Zambrini, Opportunities in quantum reservoir computing and extreme learning machines, *Adv. Quantum Technol.* **4**, 2100027 (2021).
- [27] C. M. Wilson, J. S. Otterbach, N. Tezak, R. S. Smith, A. M. Pollreno, P. J. Karalekas, S. Heidel, M. S. Alam, G. E. Crooks, and M. P. da Silva, Quantum kitchen sinks: An algorithm for machine learning on near-term quantum computers, arXiv:1806.08321 (2018).



- [28] J. García-Beni, G. L. Giorgi, M. C. Soriano, and R. Zambrini, Scalable photonic platform for real-time quantum reservoir computing, *Phys. Rev. Appl.* **20**, 014051 (2023).
- [29] V. Havlíček, A. D. Córcoles, K. Temme, A. W. Harrow, A. Kandala, J. M. Chow, and J. M. Gambetta, Supervised learning with quantum-enhanced feature spaces, *Nature (London)* **567**, 209 (2019).
- [30] G. E. Rowlands, M.-H. Nguyen, G. J. Ribeill, A. P. Wagner, L. C. G. Govia, W. A. S. Barbosa, D. J. Gauthier, and T. A. Ohki, Reservoir computing with superconducting electronics, arXiv:2103.02522 (2021).
- [31] X. Lin, Y. Rivenson, N. T. Yardimci, M. Veli, Y. Luo, M. Jarrahi, and A. Ozcan, All-optical machine learning using diffractive deep neural networks, *Science* **361**, 1004 (2018).
- [32] S. Pai, Z. Sun, T. W. Hughes, T. Park, B. Bartlett, I. A. D. Williamson, M. Minkov, M. Milanizadeh, N. Abebe, F. Morichetti, A. Melloni, S. Fan, O. Solgaard, and D. A. B. Miller, Experimentally realized in situ backpropagation for deep learning in photonic neural networks, *Science* **380**, 398 (2023).
- [33] J. Dambre, D. Verstraeten, B. Schrauwen, and S. Massar, Information processing capacity of dynamical systems, *Scientific reports* **2**, 514 (2012).
- [34] F. C. Sheldon, A. Kolchinsky, and F. Caravelli, Computational capacity of lrc, memristive and hybrid reservoirs, *Phys. Rev. E* **106**, 045310 (2022).
- [35] M. Schuld, R. Sweke, and J. J. Meyer, Effect of data encoding on the expressive power of variational quantum-machine-learning models, *Phys. Rev. A* **103**, 032430 (2021).
- [36] Y. Wu, J. Yao, P. Zhang, and H. Zhai, Expressivity of quantum neural networks, *Phys. Rev. Res.* **3**, L032049 (2021).
- [37] F. Hu, G. Angelatos, S. A. Khan, M. Vives, E. Türeci, L. Bello, G. E. Rowlands, G. J. Ribeill, and H. E. Türeci, Tackling sampling noise in physical systems for machine learning applications: Fundamental limits and eigen-tasks, *Physical Review X* **13**, 041020 (2023).
- [38] I. Ozer, M. R. Grace, and S. Guha, Reconfigurable spatial-mode sorter for super-resolution imaging, in *Conference on Lasers and Electro-Optics (CLEO)* (IEEE, 2022) pp. 1–2.
- [39] M. P. Lavery, D. J. Robertson, G. C. Berkhout, G. D. Love, M. J. Padgett, and J. Courtial, Refractive elements for the measurement of the orbital angular momentum of a single photon, *Optics express* **20**, 2110 (2012).
- [40] M. W. Beijersbergen, L. Allen, H. Van der Veen, and J. Woerdman, Astigmatic laser mode converters and transfer of orbital angular momentum, *Optics Communications* **96**, 123 (1993).
- [41] R. Ionicioiu, Sorting quantum systems efficiently, *Scientific reports* **6**, 25356 (2016).
- [42] Y. Zhou, M. Mirhosseini, D. Fu, J. Zhao, S. M. Hashemi Rafsanjani, A. E. Willner, and R. W. Boyd, Sorting photons by radial quantum number, *Physical review letters* **119**, 263602 (2017).
- [43] Y. Zhou, J. Zhao, Z. Shi, S. M. Hashemi Rafsanjani, M. Mirhosseini, Z. Zhu, A. E. Willner, and R. W. Boyd, Hermite–gaussian mode sorter, *Optics letters* **43**, 5263 (2018).
- [44] R. O’Donnell and J. Wright, Efficient quantum tomography, in *Proceedings of the forty-eighth annual ACM symposium on Theory of Computing* (2016) pp. 899–912.
- [45] J. Haah, A. W. Harrow, Z. Ji, X. Wu, and N. Yu, Sample-optimal tomography of quantum states, in *Proceedings of the forty-eighth annual ACM symposium on Theory of Computing* (2016) pp. 913–925.
- [46] T. Metger, A. Poremba, M. Sinha, and H. Yuen, Pseudorandom unitaries with non-adaptive security, arXiv preprint arXiv:2402.14803 (2024).
- [47] F. Ma and H.-Y. Huang, How to construct random unitaries, arXiv preprint arXiv:2410.10116 (2024).
- [48] T. Schuster, J. Haferkamp, and H.-Y. Huang, Random unitaries in extremely low depth, arXiv preprint arXiv:2407.07754 (2024).
- [49] S. L. Braunstein and C. M. Caves, Statistical distance and the geometry of quantum states, *Physical Review Letters* **72**, 3439 (1994).
- [50] M. G. Paris, Quantum estimation for quantum technology, *International Journal of Quantum Information* **7**, 125 (2009).

## Appendix A: Preliminary

### 1. Review of quantum-metrology-inspired superresolution

The Fisher information matrix  $F$  provides a lower bound on the variance  $\Sigma_{\vec{\theta}}$  associated with estimating unknown parameters  $\vec{\theta} = [\theta_1, \theta_2, \dots, \theta_n]$ , such that  $\Sigma_{\vec{\theta}} \geq F^{-1}$  [49, 50]. Quantum-metrology-inspired superresolution leverages the insight that a more carefully designed measurement can yield significantly higher Fisher information compared to direct imaging, when the size of the source is much smaller than the Rayleigh limit of the imaging system. Ref. [1] highlighted that, when estimating the separation between two point sources, the Fisher information from direct imaging approaches zero as the separation between the sources decreases to zero, which indicates the Rayleigh's limit. However, the Fisher information for a spatial mode demultiplexing (SPADE) measurement onto Hermite-Gaussian modes remains constant, suggesting that it is possible to circumvent Rayleigh's criterion by carefully designing the measurement strategy.

Later on, this discussion is extended to consider a general source within the Rayleigh limit. We now review the discussion in Ref. [5] using our notation in more detail for later use. A general incoherent source can be modeled as

$$\rho = \int du du_1 du_2 I(u) \psi(u - u_1) |u_1\rangle \langle u_2| \psi(u - u_2), \quad (\text{A1})$$

where  $|u\rangle = a_u^\dagger |0\rangle$  is the single photon state at position  $u$ ,  $\psi(u)$  is the PSF whose width is quantified as  $\sigma$ , such as  $\psi(u) = \exp(-u^2/4\sigma^2)/(2\pi\sigma^2)^{1/4}$ . Assume the size of the source is limited to be within  $[-L/2, L/2]$ , define  $\alpha = L/\sigma \ll 1$ , we expand the PSF

$$\psi(u_1 - u) = \sum_{n=0}^{\infty} \left( \frac{\partial^n \psi(u_1 - u)}{\partial u^n} \Big|_{u=u_0} \frac{L^n}{n!} \right) \left( \frac{u - u_0}{L} \right)^n = \sum_{n=0}^{\infty} \psi^{(n)}(u_1) \left( \frac{u - u_0}{L} \right)^n. \quad (\text{A2})$$

We can then get

$$\begin{aligned} \rho &= \sum_{m,n=0}^{\infty} \left( \int du I(u) \left( \frac{u - u_0}{L} \right)^{m+n} \right) \left( \int du_1 \psi^{(m)}(u_1) |u_1\rangle \right) \left( \int du_2 \psi^{(n)}(u_2) \langle u_2| \right) \\ &= \sum_{m,n=0}^{\infty} x_{m+n} |\psi^{(m)}\rangle \langle \psi^{(n)}| = \sum_{k=0}^{\infty} x_k \rho^{(k)}, \end{aligned} \quad (\text{A3})$$

where  $\rho^{(k)} = \sum_{m+n=k} |\psi^{(m)}\rangle \langle \psi^{(n)}|$ . We aim to construct a measurement such that, when estimating higher-order moments, the lower-order terms of  $\alpha$ , which introduce significant noise, can be canceled. This can be achieved by constructing an orthonormal measurement basis  $|b_l\rangle_l$  through the Gram-Schmidt procedure such that

$$a_{ml} = \langle \psi^{(m)} | b_l \rangle \begin{cases} = 0 & m \leq l - 1 \\ \neq 0 & m \geq l \end{cases} \quad (\text{A4})$$

The measurement is then constructed as

$$\left\{ \frac{1}{2} |\phi_{i,\pm}\rangle \langle \phi_{i,\pm}|, \frac{1}{2} |b_0\rangle \langle b_0| \right\}, \quad (\text{A5})$$

$$|\phi_{i,\pm}\rangle = (|b_i\rangle \pm |b_{i+1}\rangle)/\sqrt{2}, \quad i = 0, 1, 2, \dots \quad (\text{A6})$$

The probability of projecting onto state  $|\phi_{n,\pm}\rangle$  is

$$\begin{aligned} P_0 &= \frac{1}{2} \sum_{m=0}^{\infty} x_m \rho_{0,m,0} = \sum_{m=0}^{\infty} c_m x_m \alpha^m \\ P_{n,\pm} &= \frac{1}{4} \sum_{m=2n}^{\infty} x_m \rho_{n,m,n} + \frac{1}{4} \sum_{m=2n+2}^{\infty} x_m \rho_{(n+1),m,(n+1)} \pm \frac{1}{4} \sum_{m=2n+1}^{\infty} x_m (\rho_{n,m,(n+1)} + \rho_{(n+1),m,n}) \\ &= \sum_{m \geq 2n} c_{nm}^{\pm} x_m \alpha^m, \quad n = 0, 1, 2, 3, \dots \\ \rho_{n,m,l} &= \langle b_n | \rho^{(m)} | b_l \rangle \sim \Theta(\alpha^m), \end{aligned} \quad (\text{A7})$$

where we can find each coefficients  $c_{nm}$ . As suggested above, the probability of obtaining this outcome will, by construction, not include the lower-order terms of  $O(\alpha^{\leq 2n-1})$ . The Fisher information contributed by the basis  $|\phi_{n,\pm}\rangle$  is

$$F_{x_i x_j}^{(n)} = \begin{cases} \Theta(\alpha^{i+j-2n}) & , \quad i, j \geq 2n \\ 0 & , \quad i < 2n \quad \text{or} \quad j < 2n \end{cases} \quad (\text{A8})$$

where  $i, j, n = 0, 1, 2, \dots$ . Adding the contribution of all basis  $|\phi_{n,\pm}\rangle$ , the total Fisher information  $F = \sum_n F^{(n)}$  is given by

$$F_{x_i x_j} = \Theta(\alpha^{i+j-2\lfloor \min\{i,j\}/2 \rfloor}). \quad (\text{A9})$$

In particular, the diagonal elements  $F_{x_i x_i}$  scale as  $\Theta(\alpha^0), \Theta(\alpha^2), \Theta(\alpha^2), \Theta(\alpha^4), \Theta(\alpha^4), \dots$  for  $i = 0, 1, 2, 3, 4, \dots$ . Note that the scaling of the Fisher information in the above equation differs from that in Ref.[5] by a factor of  $\alpha^2$ . This discrepancy arises because we define the moment as  $x_k = \int du I(u)(u - u_0)^k / L^k$ , while in Ref.[5], the moment was defined as  $M_k = (\int du I(u)(u - u_0)^k)^{1/k}$ . Here,  $x_k$  is independent of  $\alpha$ , whereas  $M_k \propto \alpha$ , leading to the factor of  $\alpha^2$  difference in the Fisher information.

For a direct imaging approach, we simply project onto the state  $|u\rangle\langle u|$  to estimate the intensity at each position  $u$  on the image plane, with the probability given by

$$P_n = \sum_{m=0}^{\infty} c_{nm} x_m \alpha^m, \quad n = 0, 1, 2, 3, \dots \quad (\text{A10})$$

Note that in practical detection scenarios, it is not feasible to estimate each spatial mode individually as  $|u\rangle\langle u|$ . Instead, we measure discretized pixels, represented as  $M_n = \int_{X_n-l/2}^{X_n+l/2} dx |x\rangle\langle x|$ , where  $l$  is the size of each pixel in the direct imaging,  $X_n$  is the centroid of each pixel. Consequently, we will use a discretized version of direct imaging for both analytical and numerical discussions. And we can calculate the FI of estimating  $x_n$  as

$$F_{x_i x_j} = \Theta(\alpha^{i+j}), \quad (\text{A11})$$

which is much lower compared to the measurement constructed in Eq. A9. Specifically, the diagonal elements scale as  $F_{x_i x_i} = \Theta(\alpha^0), \Theta(\alpha^2), \Theta(\alpha^4), \Theta(\alpha^6), \Theta(\alpha^8), \dots$  for  $i = 0, 1, 2, 3, 4, \dots$ . This indicates that sensitivity can be improved by carefully designing the measurement strategy.

The measurement scheme from Ref. [5] works universally for any PSF. For the Gaussian PSF  $\psi(u) = \exp(-u^2/4\sigma^2)/(2\pi\sigma^2)^{1/4}$ , the scheme from Ref. [5] is the projective measurement  $\{\frac{1}{4}(|b_i\rangle \pm |b_{i+1}\rangle)\langle b_i| \pm \langle b_{i+1}|, \frac{1}{2}|b_0\rangle\langle b_0|\}_{i=0,1,2,\dots}$  as in Eq. A5, where  $|b_q\rangle = \int du \phi_q(u)|u\rangle$  and  $\phi_q(u) = (1/2\pi\sigma^2)^{1/4}(1/\sqrt{2^q q!})H_q(\frac{x}{\sqrt{2}\sigma})\exp(-\frac{u^2}{4\sigma^2})$ , with  $H_q$  as the Hermite polynomial. Note that the SPADE measurement first used in Ref. [1] is the projective measurement  $\{|b_q\rangle\langle b_q|\}_{q=0,1,2,3,\dots}$  when PSF is Gaussian, the measurement scheme from Ref. [5] is the projective measurement  $\{\frac{1}{4}(|b_i\rangle \pm |b_{i+1}\rangle)\langle b_i| \pm \langle b_{i+1}|, \frac{1}{2}|b_0\rangle\langle b_0|\}_{i=0,1,2,\dots}$ . For simplicity, however, we still refer to the measurement from Ref. [5] for any PSF as the SPADE method throughout the discussion. However, all the analytical results presented in this work apply to any PSF and to the measurement approach from Ref. [5].

## 2. Resolvable expressive capacity

We will use the tools of resolvable expressive capacity (REC) introduced in Ref. [37]. If our goal is approximate a function  $f(\boldsymbol{\theta})$ , define the capacity

$$C[f] = 1 - \min_W \frac{\mathbb{E}_{\boldsymbol{\theta}} \left[ \mathbb{E}_{\mathcal{X}} \left[ \left( \sum_{k=0}^{K-1} W_k \bar{\eta}_k(\boldsymbol{\theta}) - f(\boldsymbol{\theta}) \right)^2 \right] \right]}{\int f^2(\boldsymbol{\theta}) p(\boldsymbol{\theta}) d\boldsymbol{\theta}}, \quad (\text{A12})$$

where we take the expectation value for the output sample  $\mathcal{X}$  and the prior distribution  $p(\boldsymbol{\theta})$ , where  $f(\boldsymbol{\theta})$  is approximated by a linear combination of measured functions  $\bar{\eta}_k(\boldsymbol{\theta})$ . The mean squared error loss serves as an effective approximation of the first term in the Taylor expansion for a wide range of nonlinear post-processing and non-quadratic

loss functions [37]. The total REC,  $C_T = \sum_{l=0}^{\infty} C[f_l]$ , where  $\{f_l\}_l$  represents a complete and orthonormal set of basis functions, can be derived as

$$C_T = \text{Tr} \left( \left( G + \frac{1}{S} V \right)^{-1} G \right) = \sum_{k=0}^{K-1} \frac{1}{1 + \beta_k^2/S}, \quad (\text{A13})$$

$$\begin{aligned} D_{kk} &= \text{Tr} \left\{ \hat{M}_k \hat{\rho}^{(1)} \right\}, \quad G_{jk} = \text{Tr} \left\{ \left( \hat{M}_j \otimes \hat{M}_k \right) \hat{\rho}^{(2)} \right\}, \quad \hat{\rho}^{(t)} = \int \hat{\rho}(\boldsymbol{\theta})^{\otimes t} p(\boldsymbol{\theta}) d\boldsymbol{\theta}, \\ V &= D - G, \quad V \mathbf{r}_k = \beta_k^2 G \mathbf{r}_k. \end{aligned} \quad (\text{A14})$$

where  $p(\boldsymbol{\theta})$  describes our prior knowledge about the input,  $\rho(\boldsymbol{\theta})$  is the quantum state encoded with input data  $\boldsymbol{\theta}$ ,  $S$  is the number of samples,  $\{M_k\}$  is a set of  $K$  POVM elements. The total REC  $C_T$  describes the capability of approximating arbitrary functions  $f(\boldsymbol{\theta})$  using  $\bar{\eta}_k(\boldsymbol{\theta})$ . In this Letter,  $\bar{\eta}_k(\boldsymbol{\theta})$  corresponds to the observed frequency of occurrence of the  $k$ th measurement outcome and  $\mathbb{E}_{\mathcal{X}}[\bar{\eta}_k(\boldsymbol{\theta})] = \eta_k(\boldsymbol{\theta}) = P_k(\boldsymbol{\theta}) = \text{tr}(\rho(\boldsymbol{\theta})M_k)$ . A larger  $C_T$ , or smaller  $\beta_k^2$ , indicates better learning performance. Note that this theoretical framework incorporates only  $\hat{\rho}^{(t=1,2)}$ . This is because  $C[f]$  is defined based on the square error, so when deriving the equation, only the expectation and covariance of  $\bar{\eta}_k(\boldsymbol{\theta})$  are involved. Since we only need the expectation and covariance of the probability distribution,  $\hat{\rho}^{(t=1,2)}$  is sufficient.

The eigenvectors  $\mathbf{r}_k$  determines the eigentasks

$$y_k(\boldsymbol{\theta}) = \sum_j \mathbf{r}_{kj} \eta_j(\boldsymbol{\theta}), \quad (\text{A15})$$

where  $\eta_j(\boldsymbol{\theta}) = \mathbb{E}_{\mathcal{X}}[\bar{\eta}_j(\boldsymbol{\theta})]$  is probability of obtaining the  $k$ th measurement outcome. The REC of each eigentask is  $C[y_k(\boldsymbol{\theta})] = 1/(1 + \beta_k^2/S)$ . In the actual experiment, the direct measurement results yield  $\bar{\eta}_j(\boldsymbol{\theta})$ . In general, the information obtained from each  $\eta_j$  may not be independent. On the other hand, the eigentasks  $y_k$  are orthonormal in the sense of

$$\mathbb{E}_{\mathbf{u}}[y_k(\boldsymbol{\theta})y_j(\boldsymbol{\theta})] = \delta_{kj}. \quad (\text{A16})$$

Intuitively, these can be interpreted as the ‘‘independent’’ tasks with learning precision quantified by  $\beta_k^2$ . The calculation of eigentasks can give us a sense of what function is hard to be estimated for our measurement device.

## Appendix B: Two-point sources

In this section, we give more details about the calculation of imaging two-point sources using direct imaging and the binary SPADE method proposed in Ref. [1]. For the binary SPADE method, the POVM can be written as  $M_0 = |\phi_0\rangle\langle\phi_0|$ ,  $M_1 = I - M_0$ ,  $|\phi_0\rangle = \int du \phi_0(u) |u\rangle$ ,  $\phi_0(u) = \frac{1}{(2\pi\xi^2)^{1/4}} \exp\left(-\frac{u}{4\xi^2}\right)$ . We can then calculate the matrix elements of  $D, G$  for the eigenvalue problem  $V = D - G$ ,  $V \mathbf{r}_k = \beta_k^2 G \mathbf{r}_k$ .

$$D_{00} = \text{tr}(M_0 \rho^{(1)}) = \frac{4\xi\sigma}{\sqrt{(\xi^2 + \sigma^2)(\gamma^2 + 4\xi^2 + 4\sigma^2)}}, \quad D_{11} = 1 - D_{00}, \quad (\text{B1})$$

$$G_{00} = \text{tr}\left((E_0 \otimes E_0) \rho^{(2)}\right) = \frac{4\sqrt{2}\sigma^2\xi^2}{(\sigma^2 + \xi^2)^{3/2} \sqrt{\gamma^2 + 2\xi^2 + 2\sigma^2}},$$

$$G_{01} = G_{10} = \text{tr}\left((E_0 \otimes E_1) \rho^{(2)}\right) = \text{tr}\left((E_0 \otimes I) \rho^{(2)}\right) - \text{tr}\left((E_0 \otimes E_0) \rho^{(2)}\right) = D_{00} - G_{00},$$

$$G_{11} = \text{tr}\left((E_1 \otimes E_1) \rho^{(2)}\right) = \text{tr}\left(\rho^{(2)}\right) - \text{tr}\left((I \otimes E_0) \rho^{(2)}\right) - \text{tr}\left((E_0 \otimes I) \rho^{(2)}\right) + \text{tr}\left((E_0 \otimes E_0) \rho^{(2)}\right) = 1 - 2D_{00} + G_{00}, \quad (\text{B2})$$

$$D = \begin{bmatrix} D_{00} & 0 \\ 0 & D_{11} \end{bmatrix}, \quad G = \begin{bmatrix} G_{00} & G_{01} \\ G_{10} & G_{11} \end{bmatrix}, \quad (\text{B3})$$

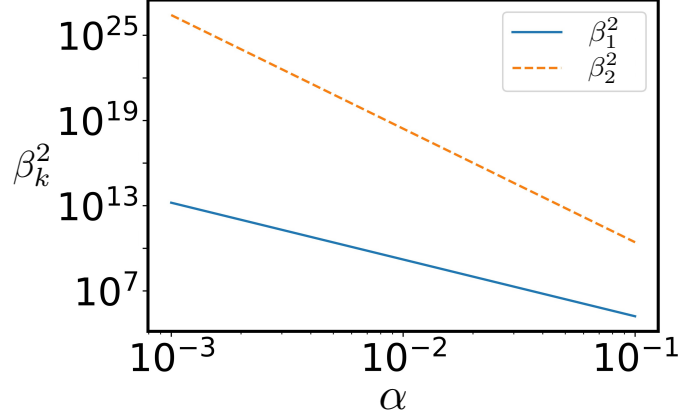


FIG. 6. Scaling of the eigenvalue  $\beta_{1,2,3}^2$  as a function of  $\alpha$  for direct imaging of two-point sources.

which then gives us the eigenvalues

$$\begin{aligned} \beta_0^2 &= 0, \\ \beta_1^2 &= \frac{-\sqrt{2}\xi\sigma(\gamma^2 + 4(\xi^2 + \sigma^2)) + \sqrt{\xi^2 + \sigma^2}\sqrt{\gamma^2 + 2(\xi^2 + \sigma^2)}\sqrt{(\xi^2 + \sigma^2)(\gamma^2 + 4(\xi^2 + \sigma^2))}}{\xi\sigma(4\sqrt{2}\xi^2 + \sqrt{2}(\gamma^2 + 4\sigma^2) - 4\sqrt{\xi^2 + \sigma^2}\sqrt{\gamma^2 + 2(\xi^2 + \sigma^2)})}. \end{aligned} \quad (\text{B4})$$

If we assume  $\gamma \ll \sigma, \xi$  and define  $\alpha = \gamma/\sigma$ , we have

$$\beta_1^2 = \frac{16(\xi - \sigma)^2(\xi^2 + \sigma^2)^2}{\xi\sigma\gamma^4} + \frac{2(\xi^2 + \sigma^2)(-8\xi\sigma + 5(\xi^2 + \sigma^2))}{\xi\sigma\gamma^2} + \frac{3}{8} \left( -4 + \frac{3\xi}{\sigma} + \frac{3\sigma}{\xi} \right) - \frac{\gamma^2}{64(\xi\sigma)} + O(\alpha^4). \quad (\text{B5})$$

The first-order term  $\Theta(\alpha^{-4})$  can be made to vanish if we choose  $\xi = \sigma$ . With this choice, the leading order of  $\beta_1^2$  becomes proportional to  $\alpha^{-2}$ .

We may want to compare this with the direct imaging case where we directly project onto each spatial mode  $\{E_x = |x\rangle \langle x|\}_x$ . We again calculate the matrix elements as

$$D_{xx} = \text{tr}(E_x \rho^{(1)}) = \frac{\sqrt{2/\pi}}{\sqrt{\gamma^2 + 4\sigma^2}} \exp[-2x^2/(\gamma^2 + 4\sigma^2)], \quad (\text{B6})$$

$$G_{xy} = \text{tr}((E_x \otimes E_y)\rho^{(2)}) = \frac{\exp\left(-\frac{x^2+y^2}{2\sigma^2}\right)}{2\sqrt{2}\pi\gamma\sigma^2\sqrt{\frac{2}{\gamma^2} + \frac{1}{\sigma^2}}} \left[ \exp\left(\frac{\gamma^2(x-y)^2}{4\sigma^2(\gamma^2 + 2\sigma^2)}\right) + \exp\left(\frac{\gamma^2(x+y)^2}{4\sigma^2(\gamma^2 + 2\sigma^2)}\right) \right]. \quad (\text{B7})$$

It is possible to numerically find  $\beta_k^2$  as shown in Fig. 6. We again choose  $\alpha = \gamma/\sigma$ . In this case, the smallest eigenvalue  $\beta_0^2 = \Theta(1)$ , followed by  $\beta_1^2 = \Theta(\alpha^{-4})$  and  $\beta_2^2 = \Theta(\alpha^{-8})$ . More details about the numerical calculation can be found in Sec. F.

## Appendix C: A single compact source (generally distributed source within the Rayleigh limit)

### 1. Direct imaging of a single compact source

We model a general incoherent source as

$$\rho = \sum_{k=0}^{\infty} x_k \rho^{(k)}, \quad (\text{C1})$$

where  $\rho^{(k)} = \Theta(\alpha^k)$ , which depends on the choice of PSF as detailed in Sec. A 1 of the supplemental and moments vector  $\vec{x} = [x_0, x_1, \dots]^T$  is our input data, i.e.  $\theta = \vec{x}$ . For direct imaging, we directly project onto each position  $|u\rangle$ , and the probability distribution for the direct imaging is given in the form of

$$P_n = \sum_{m=0}^{\infty} c_{nm} x_m \alpha^m, \quad n = 0, 1, 2, 3, \dots \quad (\text{C2})$$

Again, we measure  $M_n = \int_{X_n-l/2}^{X_n+l/2} du |u\rangle \langle u|$ , a discretized version of direct imaging for both analytical and numerical discussions. Assume we have the prior knowledge about the moments  $\vec{x} = [x_0, x_1, x_2, \dots]$  described by  $p(\vec{x})$ . The prior distribution can be derived from the knowledge that the image is selected from all possible images  $I_m(u)$ , weighted by their probabilities  $p(I_m(u))$ . Each image has a corresponding moment vector  $\vec{x}(m)$ . Therefore, the prior distribution  $p(\vec{x})$  for each moment vector  $\vec{x}$  can be calculated by weighting it according to the probabilities  $p(I_m(u))$  of all the images  $I_m(u)$  associated with the moments  $\vec{x}$ . For any moment vector  $\vec{x}$  that does not correspond to a valid image  $I_m(u)$ , or if all corresponding images  $I_m(u)$  have  $p(I_m(u)) = 0$ , we simply assume that  $p(\vec{x}) = 0$ . We define

$$d_k = \int d\vec{x} p(\vec{x}) x_k, \quad g_{k_1 k_2} = \int d\vec{x} p(\vec{x}) x_{k_1} x_{k_2}. \quad (\text{C3})$$

We can rewrite the eigenvalue problem as

$$G r_k = \lambda_k D r_k, \quad (\text{C4})$$

where  $\lambda_k = (\beta_k^2 + 1)^{-1}$ . Notice that  $D_{kk} = \int d\vec{x} p(\vec{x}) P_k(\vec{x})$  and  $G_{jk} = \int d\vec{x} p(\vec{x}) P_j(\vec{x}) P_k(\vec{x})$ . We can expand  $D$  and  $G$  as a series of  $\alpha$

$$D = \sum_{n=0}^{\infty} D^{(n)} = \sum_{n=0}^{\infty} d_n \alpha^n C_n, \quad C_n = \begin{bmatrix} c_{0n} & 0 & 0 & \dots \\ 0 & c_{1n} & 0 & \dots \\ 0 & 0 & c_{2n} & \dots \\ \dots & \dots & \dots & \dots \end{bmatrix}, \quad (\text{C5})$$

$$G = \sum_{n=0}^{\infty} G^{(n)} = \sum_{n=0}^{\infty} \alpha^n \sum_{i+j=n} g_{ij} C_i C_j^T, \quad C_i = [c_{0i}, c_{1i}, c_{2i}, \dots]^T. \quad (\text{C6})$$

We can reformulate the eigenvector problem as  $W y_k = \lambda_k y_k$ , where  $W = D^{-1/2} G D^{-1/2}$ . In the basis  $\{z_n\}_{n=0,1,2,\dots}$ , which is the orthonormal basis constructed from the set of vectors  $\{D^{-1/2} C_n\}_{n=0,1,2,\dots}$  using the Gram-Schmidt procedure, the elements of  $W$  are given by  $z_m^\dagger W z_n = \Theta(\alpha^{m+n})$ . We can intuitively predict the scaling of eigenvalues from its character polynomial

$$|\lambda I - W| = \sum_{k=0}^M (-1)^k e_k \lambda^{M-k}, \quad (\text{C7})$$

where

$$e_0 = 1, \quad e_1 = \sum \lambda_i, \quad e_2 = \sum \lambda_i \lambda_j, \quad e_3 = \sum \lambda_i \lambda_j \lambda_k, \quad \dots, \quad e_M = \prod_{i=1}^M \lambda_i. \quad (\text{C8})$$

To determine the scaling of  $\lambda_i$ , we only need to know the leading-order scaling of  $e_i$  with respect to  $\alpha$ . We observe that selecting the largest  $k$  diagonal elements  $z_n^\dagger W z_n$  provides the leading-order scaling for each  $e_k$ . This is because the contribution to each  $e_k$  from off-diagonal elements  $z_m^\dagger W z_n$  can at most share the same order of scaling with respect to  $\alpha$ . However, there is a possibility of cancellation among the contributions from the diagonal and off-diagonal elements, making this reasoning somewhat heuristic and not entirely rigorous. Essentially, we are trying to determine the scaling of  $e_k$  for a polynomial

$$(\lambda - \Theta(\alpha^0))(\lambda - \Theta(\alpha^2))(\lambda - \Theta(\alpha^4))(\lambda - \Theta(\alpha^6)) \dots \quad (\text{C9})$$

We can read from it

$$e_1 = \Theta(\alpha^0), \quad e_2 = \Theta(\alpha^{0+2}), \quad e_3 = \Theta(\alpha^{0+2+4}), \quad \dots \quad (\text{C10})$$

So, the scaling of eigenvalue

$$\lambda = \Theta(\alpha^0), \quad \Theta(\alpha^2), \quad \Theta(\alpha^4), \quad \Theta(\alpha^6), \quad \Theta(\alpha^8), \quad \dots \quad (\text{C11})$$

which implies

$$\beta_0^2 = \Theta(1), \quad \beta_1^2 = \Theta(\alpha^{-2}), \quad \beta_2^2 = \Theta(\alpha^{-4}), \quad \beta_3^2 = \Theta(\alpha^{-6}), \dots \quad (\text{C12})$$

We now try to find the scaling of eigenvalues and the eigenbasis by perturbation theory up to the  $O(\alpha^2)$  order for  $\lambda$  below,

$$\left( \sum_{n=0}^{\infty} G^{(n)} \right) \left( \sum_{n=0}^{\infty} r_k^{(n)} \right) = \left( \sum_{n=0}^{\infty} \lambda_k^{(n)} \right) \left( \sum_{n=0}^{\infty} D^{(n)} \right) \left( \sum_{n=0}^{\infty} r_k^{(n)} \right). \quad (\text{C13})$$

To the zeroth order

$$G^{(0)} r_k^{(0)} = \lambda_k^{(0)} D^{(0)} r_k^{(0)}, \quad (\text{C14})$$

$$\lambda_0^{(0)} = O(1), \quad \lambda_{j \neq 0}^{(0)} = 0, \quad r_0^{(0)} \propto [1, 1, 1, \dots, 1]^T. \quad (\text{C15})$$

We easily prove that the properly normalized eigenvector  $r_j^{(0)}$  satisfies

$$r_i^{(0)\dagger} D^{(0)} r_j^{(0)} = \delta_{ij}, \quad (\text{C16})$$

We now want to do degenerate perturbation theory in the subspace  $\text{span}\{r_{k \neq 0}^{(0)}\}$ .

$$\sum_{i+j=1} G^{(i)} r_k^{(j)} = \sum_{p+q+m=1} \lambda_k^{(p)} D^{(q)} r_k^{(m)}, \quad (\text{C17})$$

where  $k \geq 1$ . Notice that  $\lambda_{k \geq 1}^{(0)} = 0$ ,  $r.h.s = \lambda_k^{(1)} D^{(0)} r_k^{(0)}$ . Notice that  $G^{(0)}$  is a zero matrix in the subspace  $\text{span}\{r_{j \neq 0}^{(0)}\}$ ,  $l.h.s = G^{(1)} r_k^{(0)}$ . Multiplying  $r_l^{(0)\dagger}$  in both side

$$r_l^{(0)\dagger} G^{(1)} r_k^{(0)} = \lambda_k^{(1)} r_l^{(0)\dagger} D^{(0)} r_k^{(0)}, \quad (\text{C18})$$

where  $k, l \geq 1$ . Furthermore, notice that  $r_{l \geq 1}^{(0)\dagger} D^{(0)} r_0^{(0)} \propto r_{l \geq 1}^{(0)\dagger} C_0^T = 0$  and  $G^{(1)} = \alpha g_{01} C_0 C_1^T + \alpha g_{10} C_1 C_0^T$ . It is clear that the  $l.h.s$  of Eq. C18 vanishes. We thus have

$$\lambda_{k \geq 1}^{(1)} = 0. \quad (\text{C19})$$

Similarly, we can have the second order perturbation theory.

$$\sum_{i+j=2} G^{(i)} r_k^{(j)} = \sum_{p+q+m=2} \lambda_k^{(p)} D^{(q)} r_k^{(m)}. \quad (\text{C20})$$

Notice that  $\lambda_{k \geq 1}^{(0,1)} = 0$ ,  $r.h.s = \lambda_k^{(2)} D^{(0)} r_k^{(0)}$ . Notice that  $G^{(0,1)}$  is a zero matrix in the subspace  $\text{span}\{r_{j \neq 0}^{(0)}\}$ ,  $l.h.s = G^{(2)} r_k^{(0)}$ . Multiplying  $r_l^{(0)\dagger}$  in both side

$$r_l^{(0)\dagger} G^{(2)} r_k^{(0)} = \lambda_k^{(2)} r_l^{(0)\dagger} D^{(0)} r_k^{(0)} = \lambda_k^{(2)} \delta_{kl}, \quad (\text{C21})$$

$$r_l^{(0)\dagger} G^{(2)} r_k^{(0)} = \alpha^2 g_{11} r_l^{(0)\dagger} C_1 C_1^T r_k^{(0)}. \quad (\text{C22})$$

Since  $r_l^{(0)\dagger} C_1 C_1^T r_k^{(0)}$  is rank 1, we have proved that  $\lambda_1^{(2)} = \Theta(\alpha^2)$  and  $\lambda_{j \geq 2}^{(2)} = 0$ . Eigenvector  $r_1^{(0)}$  is given by orthonormalizing  $C_0^{-1} C_1$  with respect to  $r_0^{(0)} \propto C_0^{-1} C_0$ . Note this also means that  $z_n$  is the zeroth order eigenbasis for  $W y_k = \lambda_k y_k$  for the first two eigenvectors because  $\{z_n\}_{n=0,1,2,\dots}$  is the orthogonalization of  $\{D^{-1/2} C_n\}_{n=0,1,2,\dots}$ . For higher order perturbation, we need to include the higher order correction of eigenbasis  $r_k^{(j \geq 1)}$ , which becomes more involved. Therefore, we choose to stop at this point.

## 2. Image a single compact source using SPADE method

As reviewed in Sec. A 1, the probability for SPADE method takes the form of

$$P_0 = \sum_{m=0}^{\infty} c_m x_m \alpha^m, \quad P_{n\pm} = \sum_{m \geq 2n} c_{nm}^{\pm} x_m \alpha^m, \quad n = 0, 1, 2, 3, \dots \quad (\text{C23})$$

where the low order terms of  $O(\alpha^{m \leq 2n-1})$  in  $P_{n\pm}$  is cancelled out by construction. We can define

$$D = \sum_{n=0}^{\infty} D^{(n)} = \sum_{n=0}^{\infty} d_n \alpha^n C_n, \quad C_n = \Pi_{\lfloor n/2 \rfloor} C_n^0 \Pi_{\lfloor n/2 \rfloor}, \quad (\text{C24})$$

$$C_n^0 = \begin{bmatrix} c_n & 0 & 0 & 0 & 0 & \dots \\ 0 & c_{0n}^+ & 0 & 0 & 0 & \dots \\ 0 & 0 & c_{0n}^- & 0 & 0 & \dots \\ 0 & 0 & 0 & c_{1n}^+ & 0 & \dots \\ 0 & 0 & 0 & 0 & c_{1n}^- & \dots \\ \dots & \dots & \dots & \dots & \dots & \dots \end{bmatrix},$$

$$G = \sum_{n=0}^{\infty} G^{(n)} = \sum_{n=0}^{\infty} \alpha^n \sum_{i+j=n} g_{ij} C_i C_j^T, \quad C_i = \Pi_{\lfloor i/2 \rfloor} C_i^0, \quad (\text{C25})$$

$$C_i^0 = [c_i, c_{0i}^+, c_{0i}^-, c_{1i}^+, c_{1i}^-, \dots]^T, \quad \Pi_m = \begin{bmatrix} I_{2m+3} & 0 \\ 0 & 0 \end{bmatrix}.$$

We again reformulate the eigenvalue problem as  $W y_k = \lambda_k y_k$ ,  $W = D^{-1/2} G D^{-1/2}$ . Note the lower order  $D$  is not full rank. Rewriting the problem as standard eigenvalue problem avoids this difficulty. To further simplify the calculation, we will divide the matrix into blocks, the  $(m, n)$ th block is given by

$$W_{mn} = [D^{-1/2} G D^{-1/2}]_{mn}$$

$$= P_m \left( \frac{\alpha^{-m}}{\sqrt{d_{2m}}} C_{2m}^{-1/2} \left[ I - \frac{\alpha}{2} \frac{d_{2m+1}}{d_{2m}} C_{2m+1} C_{2m}^{-1} + \frac{3}{8} \alpha^2 \frac{d_{2m+1}^2}{d_{2m}^2} C_{2m+1}^2 C_{2m}^{-2} - \frac{1}{2} \alpha^2 \frac{d_{2m+2}}{d_{2m}} C_{2m+2} C_{2m}^{-1} + \dots \right] \right)$$

$$\times \sum_{i \geq 2m, j \geq 2n} \alpha^{i+j} g_{ij} C_i C_j^T \quad (\text{C26})$$

$$\times \left( \frac{\alpha^{-n}}{\sqrt{d_{2n}}} C_{2n}^{-1/2} \left[ I - \frac{\alpha}{2} \frac{d_{2n+1}}{d_{2n}} C_{2n+1} C_{2n}^{-1} + \frac{3}{8} \alpha^2 \frac{d_{2n+1}^2}{d_{2n}^2} C_{2n+1}^2 C_{2n}^{-2} - \frac{1}{2} \alpha^2 \frac{d_{2n+2}}{d_{2n}} C_{2n+2} C_{2n}^{-1} + \dots \right] \right) P_n,$$

where  $P_n = \Pi_n - \Pi_{n-1}$ ,  $\Pi_{m < 0} = 0$ . Note the leading order of block  $W_{mn}$  has lowest order  $\Theta(\alpha^{m+n})$ .

We will define the following set of orthonormal basis for convenience

$$z_{2k} \propto P_k C_{2k}^{1/2} t, \quad z_{2k+1} \perp z_{2k}, \quad z_{2k+1} \in P_k, \quad (\text{C27})$$

where  $k = 0, 1, 2, 3, \dots$ , and  $z_{2k+1}$  is the vector constructed by orthogonalize  $P_k C_{2k}^{-1/2} C_{2k+1} t$  over  $z_{2k}$ . And it should be clear that in this basis, for the  $(m, n)$ th block  $W_{mn} = P_m W P_n$ , the scaling of over  $\alpha$  is given by

$$\begin{bmatrix} \Theta(\alpha^{m+n}) & \Theta(\alpha^{m+n+1}) \\ \Theta(\alpha^{m+n+1}) & \Theta(\alpha^{m+n+2}) \end{bmatrix}, \quad (\text{C28})$$

To find the scaling of eigenvalues, we again try to observe the structure of the character polynomial  $|\lambda I - W| = \sum_{k=0}^M (-1)^k e_k \lambda^{M-k}$ , its coefficients now has the form of

$$e_1 = \Theta(\alpha^0), \quad e_2 = \Theta(\alpha^{0+2}), \quad e_3 = \Theta(\alpha^{0+2+2}),$$

$$e_4 = \Theta(\alpha^{0+2+2+4}), \quad e_5 = \Theta(\alpha^{0+2+2+4+4}), \dots \quad (\text{C29})$$

So, the scaling of eigenvalue is

$$\beta_0^2 = \Theta(1), \beta_1^2 = \Theta(\alpha^{-2}), \beta_2^2 = \Theta(\alpha^{-2}), \beta_3^2 = \Theta(\alpha^{-4}), \beta_4^2 = \Theta(\alpha^{-4}), \dots \quad (\text{C30})$$



We now calculate the eigenvalues and eigenbasis based on perturbation theory. We can write  $W$  as a series of  $\alpha$ ,

$$W = \sum_{n=0}^{\infty} W^{(n)} \alpha^n. \quad (\text{C31})$$

The zeroth order term

$$W^{(0)} \propto P_0 \mathcal{C}_0^{1/2} t t^T \mathcal{C}_0^{1/2} P_0, \quad (\text{C32})$$

where  $t = [1, 1, 1, \dots]^T$ . Using perturbation theory,

$$W^{(0)} y_k^{(0)} = \lambda_k^{(0)} y_k^{(0)}, \quad (\text{C33})$$

it is clear that

$$\lambda_0 = \Theta(1), \quad y_0^{(0)} \propto P_0 \mathcal{C}_0^{1/2} t \propto z_0. \quad (\text{C34})$$

Since we have  $r_i = D^{-1/2} y_i$ , we find that

$$r_0^{(0)} \propto P_0 t. \quad (\text{C35})$$

Obviously, we have

$$\lambda_{i \neq 0}^{(0)} = 0. \quad (\text{C36})$$

Furthermore, since  $W^{(0)}$  is rank one, we will find the proper first order approximation to eigenvector  $y_{i \geq 1}^{(0)}$  as a linear combination of  $z_{i \geq 1}$  in the higher order perturbation discussion.

With this choice of  $z_k$ , we can continue the calculation for  $\Theta(\alpha)$  terms.

$$W^{(1)} y_k^{(0)} + W^{(0)} y_k^{(1)} = \lambda_k^{(1)} y_k^{(0)}, \quad k \geq 1. \quad (\text{C37})$$

If we apply  $(z_{j \geq 1})^T$  from the left and insert  $y_k^{(0)} = \sum_{m=1}^{\infty} a_{km}^{(0)} z_m$ , we get

$$\sum_{m=1}^{\infty} \left( (z_j)^T W^{(1)} z_m - \delta_{mj} \lambda_k^{(1)} \right) a_{km}^{(0)} = 0, \quad (\text{C38})$$

where we have used the fact that  $W^{(0)} z_{i \geq 1} = 0$ , which is because of our construction in Eq. C27 and  $W^{(0)} \sim P_0 \mathcal{C}_0^{1/2} t t^T \mathcal{C}_0^{1/2} P_0$ . Since  $W^{(1)}$  has terms proportional to

$$P_0 \mathcal{C}_0^{1/2} t t^T \mathcal{C}_1 \mathcal{C}_0^{-1/2} P_0, \quad P_0 \mathcal{C}_0^{-1/2} \mathcal{C}_1 t t^T \mathcal{C}_0^{1/2} P_0, \quad P_0 \mathcal{C}_0^{1/2} t t^T \mathcal{C}_2 \mathcal{C}_0^{-1/2} P_1, \quad P_1 \mathcal{C}_0^{-1/2} \mathcal{C}_2 t t^T \mathcal{C}_0^{1/2} P_0, \quad (\text{C39})$$

and  $z_{k \geq 1}$  to orthogonal to  $y_0^{(0)} \propto P_0 \mathcal{C}_0^{1/2} t$ , we have  $(z_j)^T W^{(1)} z_m = 0$  for  $j, m \geq 1$ .

$$\lambda_k^{(1)} = 0 \quad \text{for } k \geq 1. \quad (\text{C40})$$

We then consider the  $\Theta(\alpha^2)$  terms

$$W^{(2)} y_k^{(0)} + W^{(1)} y_k^{(1)} + W^{(0)} y_k^{(2)} = \lambda_k^{(2)} y_k^{(0)}, \quad k \geq 1. \quad (\text{C41})$$

Apply  $z_{j \geq 1}$  from left,

$$\sum_{m=1}^{\infty} \left( (z_j)^T W^{(2)} z_m - \delta_{mj} \lambda_k^{(2)} \right) a_{km}^{(0)} = 0, \quad (\text{C42})$$

where we have used the fact that  $z_{i \geq 1} W^{(0)} z_{j \geq 1} = z_{i \geq 1} W^{(1)} z_{j \geq 1} = 0$  as argued above. Since  $W^{(2)}$  has terms proportional to

$$P_0 \mathcal{C}_1 \mathcal{C}_0^{-1/2} t t^T \mathcal{C}_1 \mathcal{C}_0^{-1/2} P_0, \quad P_1 \mathcal{C}_2^{1/2} t t^T \mathcal{C}_2^{1/2} P_1, \quad P_0 \mathcal{C}_1 \mathcal{C}_0^{-1/2} t t^T \mathcal{C}_2^{1/2} P_1, \quad P_0 \mathcal{C}_1 \mathcal{C}_0^{-1/2} t t^T \mathcal{C}_2^{1/2} P_1, \quad (\text{C43})$$

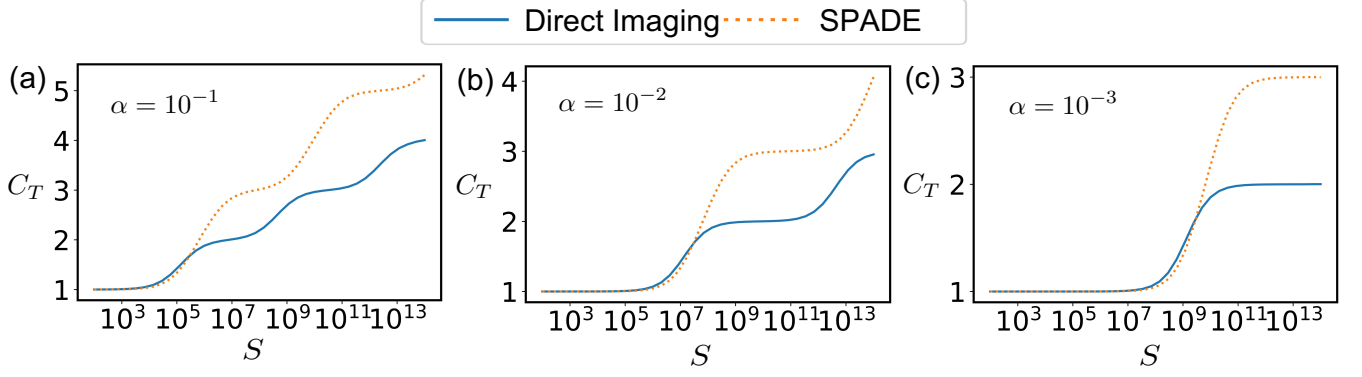


FIG. 7. Total REC  $C_T$  for direct imaging and the SPADE method as a function of  $S$ , when imaging one generally distributed compact source with different  $\alpha$ .

This shows

$$\lambda_{1,2}^{(2)} \neq 0, \quad \lambda_{k \geq 3}^{(2)} = 0, \quad (\text{C44})$$

and also provides the leading order approximation to  $y_{1,2}^{(0)}$  as a linear combination of  $z_{1,2}$ . By the orthogonality condition, we must have  $y_{i > 3}^{(0)} \perp z_{j \leq 2}$ .

We can then consider the  $\Theta(\alpha^3)$  terms

$$W^{(3)}y_k^{(0)} + W^{(2)}y_k^{(1)} + W^{(1)}y_k^{(2)} + W^{(0)}y_k^{(3)} = \lambda_k^{(3)}y_k^{(0)}, \quad k \geq 3. \quad (\text{C45})$$

We apply  $(z_{j \geq 3})^T$  from the left

$$\sum_{m=3}^{\infty} a_{km}^{(0)}(z_j)^T W^{(3)}z_m + \sum_{m=1}^{\infty} a_{km}^{(1)}(z_j)^T W^{(2)}z_m = \lambda_k^{(3)}a_{kj}^{(0)}. \quad (\text{C46})$$

Analyzing each terms of  $W^{(2)}$  and  $W^{(3)}$ , we conclude the left hand side vanishes and this shows

$$\lambda_{k \geq 3}^{(3)} = 0. \quad (\text{C47})$$

We demonstrate that  $\beta_k^2$  acts as the threshold for the stepwise increase in the total REC,  $C_T$ , as illustrated in Fig. 7 for different values of  $\alpha$  separately. For direct imaging,  $C_T$  increases by 1 at each step, while for the SPADE method,  $C_T$  increases by 2 per step, as expected. Moreover, as  $\alpha$  decreases, the plateau regions become more pronounced.

### 3. Deviation of the approximated eigenbasis from the actual eigenbasis

In this section, we want to verify the deviation of the approximated eigenbasis  $\hat{y}_k$  from the actual eigenbasis  $y_k$  vanishes as  $\alpha \rightarrow 0$ . In the direct imaging case, we predicted above that  $\{z_n\}_{n=0,1,2,\dots}$ , which is the orthonormal basis constructed from the set of vectors  $\{D^{-1/2}C_n\}_{n=0,1,2,\dots}$  using the Gram-Schmidt procedure, are the approximated eigenvector  $\hat{y}_k = z_k$  for actual eigenvectors  $y_k$ , which is confirmed as shown in Fig. 8(a). For the SPADE method, we predicted above that the approximated eigenvector  $\hat{y}_0 = z_0$ , each  $\hat{y}_{k \geq 1}$  is the linear combination of  $z_{2\lceil k/2 \rceil - 1}$  and  $z_{2\lceil k/2 \rceil}$  in Eq. C27. The coefficients in the linear combination of the two bases depend on the specific values of  $g_{ij}$  and  $d_i$ . We choose  $\hat{y}_0 = z_0$  and employ a least squares approach to fit each  $\hat{y}_{k \geq 1}$  with the two bases  $z_{2\lceil k/2 \rceil - 1}$  and  $z_{2\lceil k/2 \rceil}$  in Eq. C27. The deviation is illustrated in Fig. 8(b). In both cases, as  $\alpha \rightarrow 0$ , the actual eigenbasis  $y_k$  increasingly aligns with the eigenvectors  $\hat{y}_k$  described above. For the numerical calculations, we select the PSF as  $\psi(u) = \exp(-u^2/4\sigma^2)/(2\pi\sigma^2)^{1/4}$ . The coefficients  $d$  and  $g$  are chosen by randomly generating a set of images and assuming that these images appear with equal probability, which then can be used to  $d$  and  $g$  with the corresponding moments vector of each image as detailed in Sec. F.

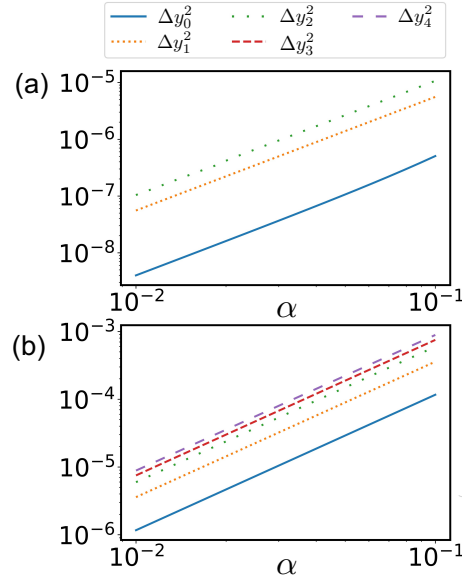


FIG. 8. Deviation of the approximated eigenvector  $\hat{y}_k$  from the actual eigenbasis  $y_k$ , the deviation is defined as the squared norm of difference between two normalized vectors  $\Delta y_k^2 = |\hat{y}_k - y_k|^2$ , for eigenvalue problems  $W y_k = \lambda_k y_k$ , where  $W = D^{-1/2} G D^{-1/2}$ . We consider the imaging of one compact source using (a) direct imaging (b) SPADE method.

#### Appendix D: Imaging general source extended outside the Rayleigh limit

In the above discussion, we have consistently assumed the size of one compact source is much smaller than the Rayleigh limit of our lens. However, in practice, the source size can exceed the Rayleigh limit, and we still need to quantify imaging performance in such cases. In this subsection, we focus on quantifying imaging performance using the REC under these conditions.

To illustrate this, we perform the following numerical calculation: we randomly generate a general source of size  $L$  consisting of  $N_{\max}$  discrete pixels, with each pixel assigned a random value between 0 and 1. We then normalize the intensity distribution  $I(u)$  such that  $\sum_u I(u) = 1$ . By repeatedly generating the intensity distribution  $I(u)$  in this manner for  $W$  times, we simulate the case where we do not have any prior knowledge of the source. For all the numerical calculation for imaging general source outside the Rayleigh limit, we use  $N_{\max} = 200$ ,  $W = 200$ . Assuming the PSF is given by  $\psi(u) = (2\pi\sigma^2)^{-1/4} \exp(-u^2/(4\sigma^2))$ , we provide a plot of  $C_T$  as a function of  $S$  on a logarithmic scale in Fig. 9. As discussed in the main text, in the case beyond resolving multiple compact sources where the sources are not localized in a few compact regions, the increase in  $C_T$  no longer exhibits the stepwise behavior. We also demonstrate that the total REC  $C_T$  roughly linearly increases with the size of source  $L$  in Fig. 10. The ratio of  $C_T/L$  roughly approaches 1 but slightly decreases as  $L$  increases in this model. In Fig. 11, we plot the total REC  $C_T$  as a function of  $\sigma$ , where our numerical results indicate that  $C_T$  approximately follows  $C_T \propto \sigma^{-0.9}$  for the model considered here. All the above calculations are performed for a single instance of randomly generated prior information. However, in Fig. 12, we present results from three consecutive executions of the calculation with  $N_{\max} = 200$  and  $W = 200$ , where each execution randomly generates a different instance of prior information. Despite the variation in prior information, we observe negligible differences in the calculation results.

#### Appendix E: Imaging multiple compact sources

The state from multiple compact sources is given by

$$\rho = \sum_{q=1}^Q \int du du_1 du_2 I_q(u) \psi(u - u_1) |u_1\rangle \langle u_2| \psi^*(u - u_2), \quad (\text{E1})$$

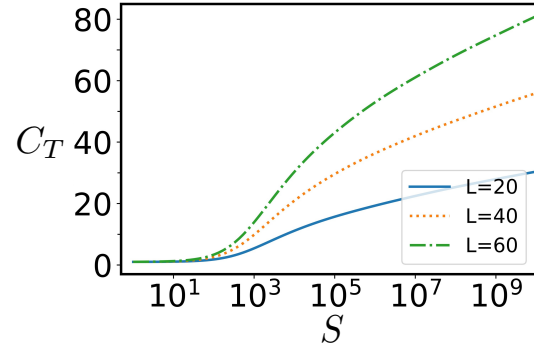


FIG. 9. Total REC  $C_T$  for direct imaging of general source extended outside the Rayleigh limit as a function of  $S$  in log scale for source with size  $L = 20, 40, 60$ .  $\sigma = 1$ .

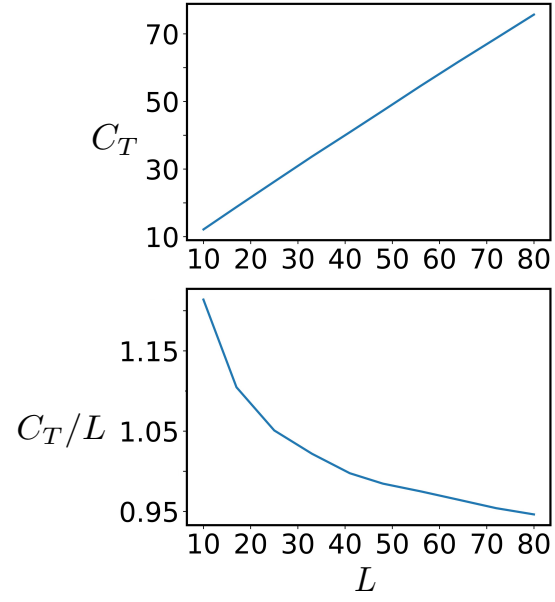


FIG. 10. Total REC  $C_T$  for direct imaging of general source extended outside the Rayleigh limit as a function of  $L$  and the ratio  $C_T/L$  as a function of  $L$ .  $\sigma = 1$ ,  $S = 10^7$ .

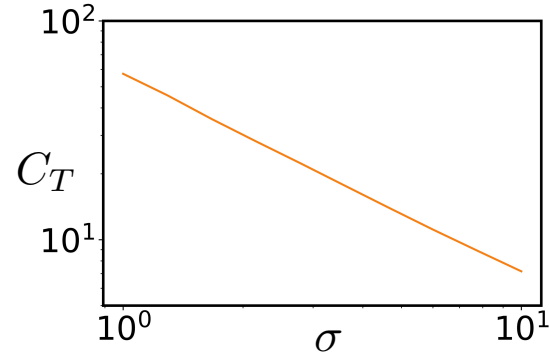


FIG. 11. Total REC  $C_T$  for direct imaging of general source extended outside the Rayleigh limit as a function of  $\sigma$ . Both axes are plotted on a logarithmic scale.  $L = 120$ ,  $S = 10^4$ .

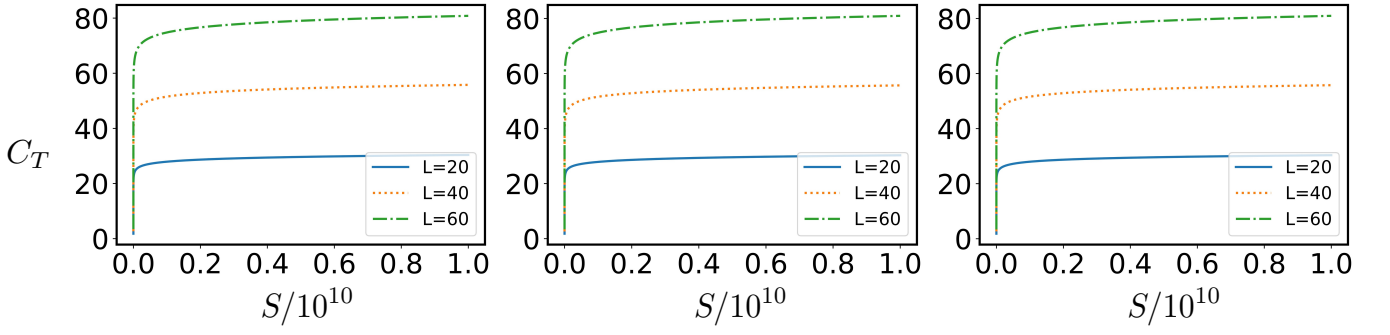


FIG. 12. Three consecutive executions of the calculation of total REC  $C_T$  for direct imaging of general source extended outside the Rayleigh limit as a function of  $S$  for source with size  $L = 20, 40, 60$ .  $\sigma = 1$ .

where  $Q$  is the number of compact sources,  $I_q(u)$  is the intensity distribution for  $q$ th compact source. We can expand the PSF near the centroid  $u_q$  of  $q$ th source

$$\begin{aligned} \psi(u_1 - u) &= \sum_{n=0}^{\infty} \left( \frac{\partial^n \psi(u_1 - u)}{\partial u^n} \Big|_{u=u_q} \frac{L_q^n}{n!} \right) \left( \frac{u - u_q}{L_q} \right)^n \\ &= \sum_{n=0}^{\infty} \psi_q^{(n)}(u_1) \left( \frac{u - u_q}{L_q} \right)^n, \end{aligned} \quad (\text{E2})$$

where  $L_q$  is the size of  $q$ th source.

$$\begin{aligned} \rho &= \sum_{q=1}^Q \sum_{m,n=0}^{\infty} x_{m+n,q} |\psi_q^{(m)}\rangle \langle \psi_q^{(n)}|, \\ |\psi_q^{(m)}\rangle &= \int du \psi_q^{(m)}(u) |u\rangle, \end{aligned} \quad (\text{E3})$$

where  $x_{n,q} = \int du I_q(u) \left( \frac{u - u_q}{L_q} \right)^n$  is the  $n$ th moment for the  $q$ th source.

### 1. Direct imaging

If we have  $Q$  compact sources, direct imaging will have the probability distribution in the following form

$$P_n = \sum_{q=1}^Q \sum_{m=0}^{\infty} c_{nmq} x_{mq} \alpha_q^m. \quad (\text{E4})$$

Again, we measure a discretized version of direct imaging for both analytical and numerical discussions  $M_n = \int_{X_n - l/2}^{X_n + l/2} du |u\rangle \langle u|$ . Notice that  $\alpha_q = L_q/\sigma$  can be different. But in the following, we will redefine the coefficients  $c_{nmq}$  involves the difference between  $L_q$  for different sources and have  $\alpha_q = \alpha$ . We will numerically explore the case where  $\alpha_q$  differs significantly and cannot be incorporated into the coefficients  $c_{nmq}$  below.

$$\begin{aligned} D &= \sum_{n=0}^{\infty} D^{(n)} = \sum_{n=0}^{\infty} \alpha^n \sum_{q=1}^Q d_{nq} C_{nq}, \quad C_{nq} = \text{diag}(C_{nq}), \quad C_{nq} = [c_{0nq}, c_{1nq}, c_{2nq}, \dots]^T, \\ G &= \sum_{n=0}^{\infty} G^{(n)} = \sum_{n=0}^{\infty} \alpha^n \sum_{n_1+n_2=n} \sum_{q_1, q_2=1}^Q g_{n_1 q_1, n_2 q_2} C_{n_1 q_1} C_{n_2 q_2}^T, \\ g_{n_1 q_1, n_2 q_2} &= \int d\vec{x} p(\vec{x}) x_{n_1 q_1} x_{n_2 q_2}, \quad d_{nq} = \int d\vec{x} p(\vec{x}) x_{nq}. \end{aligned} \quad (\text{E5})$$

where  $\text{diag}(C_{nq})$  denotes a diagonal matrix with the diagonal elements being the elements of  $C_{nq}$ . If we choose a set of basis  $z_n$  as the Gram-Schmidt orthogonalization of  $D_0^{-1/2}C_{mq}$ , we can then express the matrix  $W = D^{-1/2}GD^{-1/2}$  in the basis of  $z_n$  and divide it into  $Q \times Q$  blocks. In this block structure, the  $(m, n)$ th block scales as  $\Theta(\alpha^{m+n})$ . We can then examine the structure of the characteristic polynomial  $|\lambda I - W| = \sum_{k=0}^M (-1)^k e_k \lambda^{M-k}$ , where the coefficients  $e_k$  now take the form of

$$e_1 = \Theta(\alpha^0), \dots, e_Q = \Theta(\alpha^0), e_{Q+1} = \Theta(\alpha^{0+2}), \dots, e_{2Q} = \Theta(\alpha^{0+2}), e_{2Q+1} = \Theta(\alpha^{0+2+4}), \dots, e_{3Q} = \Theta(\alpha^{0+2+4}), \dots \quad (\text{E6})$$

So, the scaling of eigenvalue is

$$\beta_{0 \leq i \leq Q-1}^2 = \Theta(1), \quad \beta_{Q \leq i \leq 2Q-1}^2 = \Theta(\alpha^{-2}), \quad \beta_{2Q \leq i \leq 3Q-1}^2 = \Theta(\alpha^{-4}), \dots \quad (\text{E7})$$

## 2. Separate SPADE method

If we naively apply the SPADE method [5] to each compact source, which will be referred as the separate SPADE method. In other word, we use the POVM

$$\left\{ \frac{1}{2Q} |\phi_{q,m,\pm}\rangle \langle \phi_{q,m,\pm}|, \frac{1}{2Q} |b_{q,0}\rangle \langle b_{q,0}| \right\}_{q=1,2,\dots,Q, m=0,1,2,\dots,\infty}, \quad (\text{E8})$$

where  $\{|b_{q,m}\rangle\}_{m=0,1,2,\dots,\infty}$  is given by the Gram-Schmidt orthogonalization of set  $\{|\psi_q^{(m)}\rangle\}_{m=0,1,2,\dots,\infty}$ , and  $|\phi_{q,m,\pm}\rangle = \frac{1}{\sqrt{2}}(|b_{q,m}\rangle \pm |b_{q,m+1}\rangle)$ . We add the normalization factor  $1/Q$  to our POVM.

An immediate issue arises: nearby compact sources can disrupt the construction of separate SPADE method. This occurs because the designed measurement relies on canceling out lower-order terms of  $O(\alpha^n)$  through careful design. However, if other compact sources are too close, they may contribute terms that are much larger than  $O(\alpha^n)$ , undermining the effectiveness of the superresolution technique.

In general, when all compact sources are sufficiently far apart, superresolution can still be achieved. However, when the sources are too close together, the probability distribution of separate SPADE method will resemble that of direct imaging, as described in Eq. E4. To be more specific, if we choose the PSF as  $\psi(u) = \exp(-u^2/4\sigma^2)/(2\pi\sigma^2)^{1/4}$ , the threshold for achieving superresolution is determined by whether  $\alpha^n \gg \exp(-L^2/\sigma^2)$ , where  $n$  is determined by the order of the measured moments, and  $\exp(-L^2/\sigma^2)$  represents the contribution from nearby compact sources.

## 3. Orthogonalized SPADE method

With the construction of orthonormal basis  $|b_j^{(l)}\rangle$  from the Gram-Schmidt procedure such that

$$a_{mk,lj} = \langle \psi_k^{(m)} | b_j^{(l)} \rangle \begin{cases} = 0 & m \leq l-1 \\ = 0 & m = l \ \& \ k \leq j-1 \\ \neq 0 & \text{otherwise} \end{cases} \quad (\text{E9})$$

Choose POVM as

$$\left\{ \frac{1}{2} |\phi_{j,\pm}^{(l)}\rangle \langle \phi_{j,\pm}^{(l)}|, \frac{1}{2} |b_j^{(0)}\rangle \langle b_j^{(0)}| \right\}_{j=1,2,\dots,Q, l=0,1,2,\dots,\infty}, \quad (\text{E10})$$

where

$$|\phi_{j,\pm}^{(l)}\rangle = \frac{1}{\sqrt{2}} \left( |b_j^{(l)}\rangle \pm |b_j^{(l+1)}\rangle \right), \quad j = 1, 2, 3, \dots, Q, \quad l = 0, 1, 2, \dots, \infty \quad (\text{E11})$$

Then, the probability distribution

$$P_{0,j} = \frac{1}{2} \langle b_j^{(0)} | \rho | b_j^{(0)} \rangle = \sum_{q=1}^Q \sum_{n=0}^{\infty} c_{jnq} x_{nq} \alpha^n, \quad (\text{E12})$$

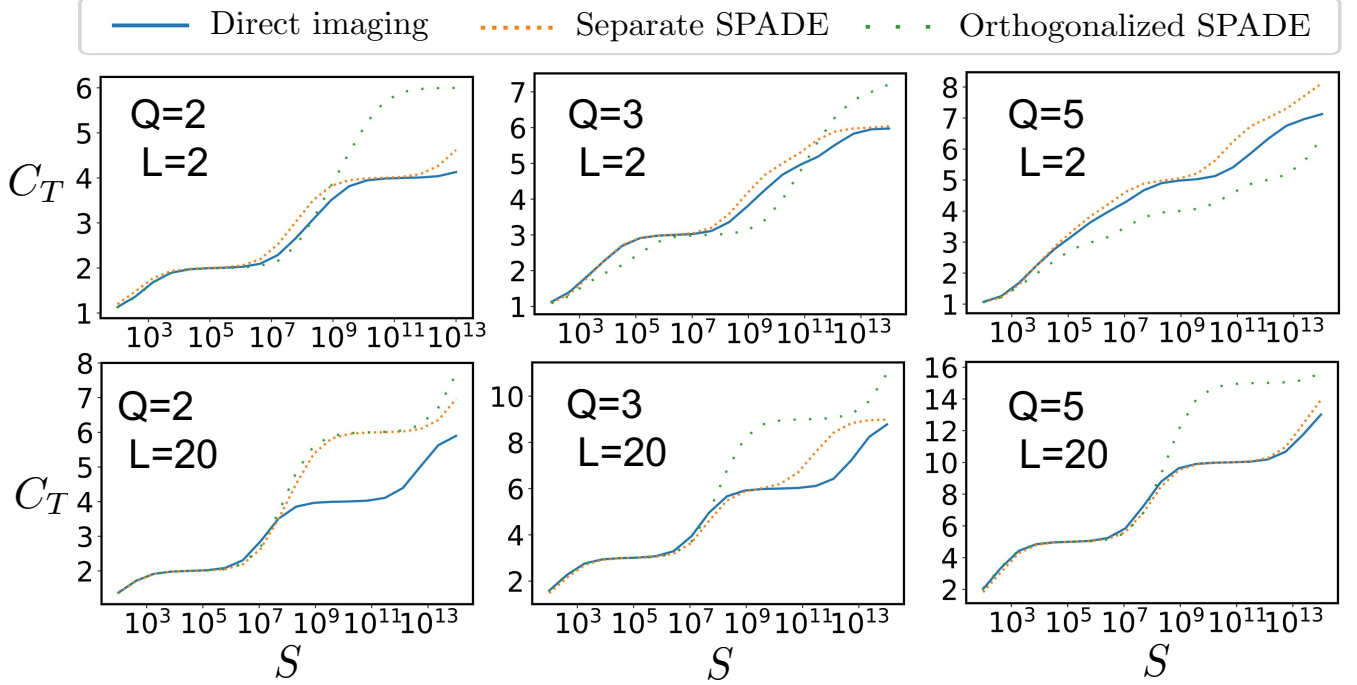


FIG. 13. Total REC  $C_T$  of imaging  $Q$  compact sources for direct imaging, separate SPADE method and orthogonalized SPADE method as a function of  $S$ .  $\alpha = 10^{-2}$ ,  $\sigma = 1$ . We consider two different  $L$  and different number of compact source  $Q$ .

$$P_{l,j,\pm} = \frac{1}{2} \langle \phi_{j\pm}^{(l)} | \rho | \phi_{j\pm}^{(l)} \rangle = \sum_{q=1}^Q \sum_{n=2l}^{\infty} c_{ljnq}^{\pm} x_{nq} \alpha^n, \quad (\text{E13})$$

$$c_{ljnq}^{\pm} = \frac{1}{4} \sum_{m=0}^n \left( a_{pq,lj} a_{mq,lj}^* + a_{pq,(l+1)j} a_{mq,(l+1)j}^* \pm a_{pq,(l+1)j} a_{mq,lj}^* \pm a_{pq,lj} a_{mq,(l+1)j}^* \right) / \alpha^n, \quad p = n - m. \quad (\text{E14})$$

We set up the REC calculation as

$$D = \sum_{n=0}^{\infty} D^{(n)} = \sum_{n=0}^{\infty} \alpha^n \sum_{q=1}^Q d_{nq} C_{nq}, \quad C_{nq} = \Pi_{nq} C_{nq}^0 \Pi_{nq}, \quad (\text{E15})$$

$$C_{nq}^0 = \text{diag}(C_{nq}^0), \quad d_{nq} = \int d\vec{x} p(\vec{x}) x_{nq}, \quad (\text{E16})$$

$$G = \sum_{n=0}^{\infty} G^{(n)} = \sum_{n=0}^{\infty} \alpha^n \sum_{n_1+n_2=n} \sum_{q_1, q_2=1}^Q g_{n_1 q_1, n_2 q_2} C_{n_1 q_1} C_{n_2 q_2}^T, \quad (\text{E17})$$

$$C_{nq} = \Pi_{nq} C_{nq}^0, \quad g_{n_1 q_1, n_2 q_2} = \int d\vec{x} p(\vec{x}) x_{n_1 q_1} x_{n_2 q_2}, \quad (\text{E18})$$

$$C_{nq}^0 = [c_{1nq}, c_{2nq}, \dots, c_{Qnq}, c_{01nq}^+, c_{01nq}^-, c_{02nq}^+, c_{02nq}^-, \dots, c_{0Qnq}^+, c_{0Qnq}^-, c_{11nq}^+, c_{11nq}^-, c_{12nq}^+, c_{12nq}^-, \dots, c_{1Qnq}^+, c_{1Qnq}^-, \dots]^T, \quad (\text{E19})$$

$$\Pi_{nq} = \begin{bmatrix} I_{2\lfloor n/2 \rfloor + 1} \otimes I_Q & 0 & 0 \\ 0 & I_2 \otimes Q_q & 0 \\ 0 & 0 & 0 \end{bmatrix}, \quad Q_q = \begin{bmatrix} I_q & 0 \\ 0 & 0 \end{bmatrix}. \quad (\text{E20})$$

We can again give an intuitive argument as in Sec. C1 and Sec. C2 about the scaling of eigenvalues  $\beta_k^2$  based on characteristic polynomial. Define  $P_m = \Pi_{2m,Q} - \Pi_{2(m-1),Q}$ ,  $\Pi_{m<0,k} = 0$ . In the  $2Q$  dimensional subspace in the support of  $P_m$ , we have vectors  $P_m C_{2m,q}$ ,  $P_m C_{2m+1,q}$ ,  $q = 1, 2, 3, \dots, Q$ ,  $m = 0, 1, 2, \dots, \infty$ . We will define the set of orthonormal basis  $z_{2m+1,q}$ ,  $z_{2m+2,q}$  for convenience such that  $z_{2m+1,q}$  is the Gram-Schmidt orthogonalization of all of

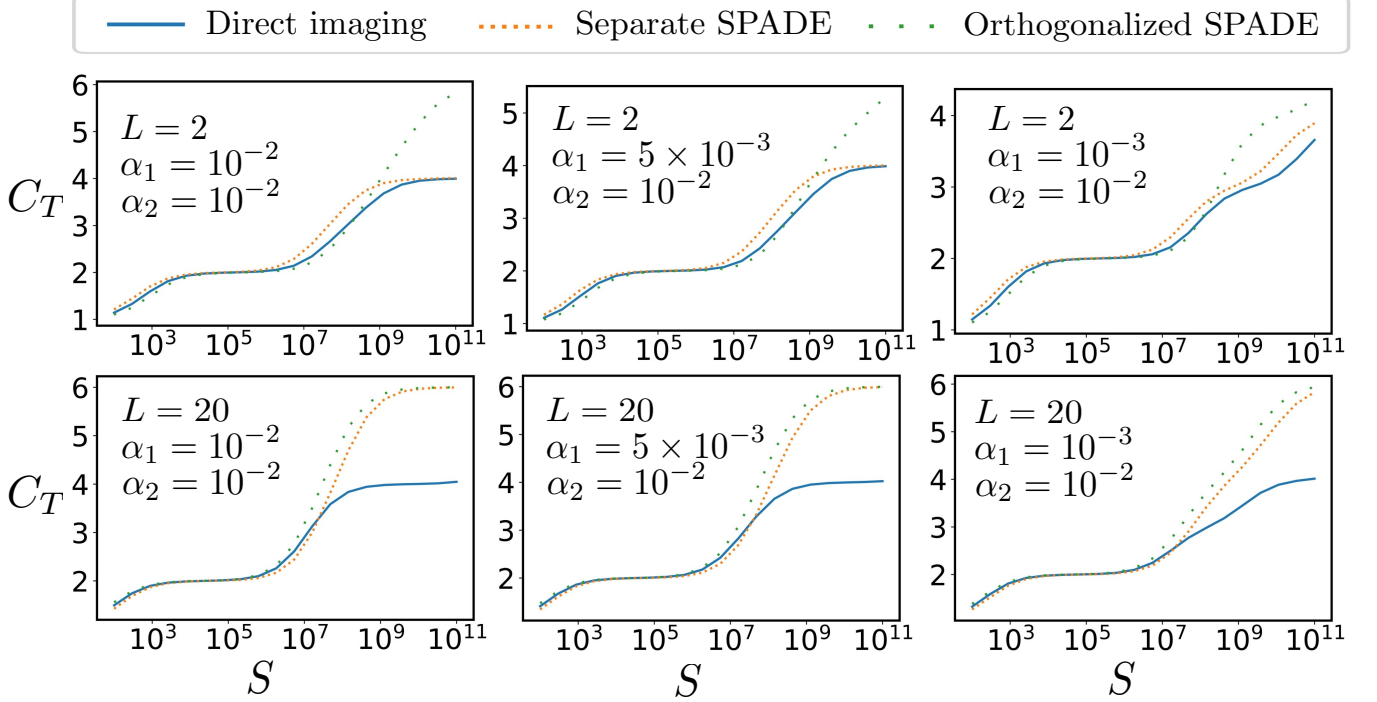


FIG. 14. Total REC  $C_T$  for direct imaging, separate SPADE method and orthogonalized SPADE method as a function of  $S$ . Assume we are imaging two compact sources  $Q = 2$ ,  $\sigma = 1$ . We consider two different  $L$  and assume the size of the two compact source is  $\alpha_1, \alpha_2$ , which can be different.

the  $\{P_m C_{2m,q}\}_{q=1,2,3,\dots,Q}$  and  $z_{2m+2,q}$  is the Gram-Schmidt orthogonalization of all of the  $\{P_m C_{2m+1,q}\}_{q=1,2,3,\dots,Q}$  while keeping orthogonal to  $\{P_m C_{2m,q}\}_{q=1,2,3,\dots,Q}$ . Then, it should be clear that in this basis, for the  $(m_1, m_2)$ th block  $W_{m_1, m_2} = P_{m_1} W P_{m_2}$ , the scaling of over  $\alpha$  is given by

$$\begin{bmatrix} W_{m_1+m_2} & W_{m_1+m_2+1} \\ W_{m_1+m_2+1} & W_{m_1+m_2+2} \end{bmatrix}, \quad (\text{E21})$$

where each block  $W_n$  is a  $Q \times Q$  matrix scaling as  $\Theta(\alpha^n)$ . To find the scaling of eigenvalues, we again try to observe the structure of the character polynomial  $|\lambda I - W| = \sum_{k=0}^M (-1)^k e_k \lambda^{M-k}$ , its coefficients now has the form of

$$\begin{aligned} e_1 &= \Theta(\alpha^0), \dots, e_Q = \Theta(\alpha^0), \\ e_{Q+1} &= \Theta(\alpha^{0+2}), \dots, e_{3Q} = \Theta(\alpha^{0+4Q}), \\ e_{3Q+1} &= \Theta(\alpha^{0+4Q+4}), \dots, e_{5Q} = \Theta(\alpha^{0+4Q+8Q}), \dots \end{aligned} \quad (\text{E22})$$

So, the scaling of eigenvalue is

$$\beta_{0 \leq i \leq Q-1}^2 = \Theta(1), \quad \beta_{Q \leq i \leq 3Q-1}^2 = \Theta(\alpha^{-2}), \quad \beta_{3Q \leq i \leq 5Q-1}^2 = \Theta(\alpha^{-4}), \dots \quad (\text{E23})$$

In Fig. 13, we present the case where  $\alpha = 10^{-2}$  is fixed, and different numbers of compact sources  $Q$  are considered, with the centroids of these  $Q$  sources evenly distributed over  $[-L/2, L/2]$ . The figure shows that when the number of sources  $Q$  exceeds roughly  $L/Q$ , the stepwise increase in  $C_T$  becomes smoothed out. Note that when we fix  $L = 20$ , the two sources in the case of  $Q = 2$  are sufficiently far apart. However, as  $Q$  increases to 3 or 5, the distance between the sources decreases, making the orthogonalization method more advantageous in these cases. In Fig. 14, we consider the case where  $Q = 2$ , but  $\alpha_1$  and  $\alpha_2$  take different values for the two compact sources. It is evident that the difference in  $\alpha_i$  between the compact sources also smooths out the stepwise increase in  $C_T$  by introducing smaller steps with varying thresholds. The prior knowledge about the moments are again chosen by randomly generating a set of images as in detailed in Sec. F.



#### 4. Implementation of the orthogonalized SPADE method

When there are two compact sources located in  $u_1$  and  $u_2$  respectively and the PSF is given by  $\psi(u) = \exp(-u^2/4\sigma^2)/(2\pi\sigma^2)^{1/4}$ , for the separate SPADE measurement, the POVM as in Eq. E8 is  $\left\{ \frac{1}{2Q} |\phi_{q,m,\pm}\rangle \langle \phi_{q,m,\pm}|, \frac{1}{2Q} |b_{q,0}\rangle \langle b_{q,0}| \right\}_{q=1,2,\dots,Q, m=0,1,2,\dots,\infty}$ , where  $|\phi_{q,m,\pm}\rangle = \frac{1}{\sqrt{2}}(|b_{q,m}\rangle \pm |b_{q,m+1}\rangle)$ . We can calculate the wavefunction  $|b_{q,m}\rangle = \int du b_{q,m}(u) |u\rangle$  as

$$b_{q,0}(u) = \frac{\exp(-(u-u_q)^2/4\sigma^2)}{(2\pi\sigma^2)^{1/4}}, \quad b_{q,1}(u) = \frac{(u-u_q)\exp(-(u-u_q)^2/4\sigma^2)}{(2\pi)^{1/4}\sigma^{3/2}}, \quad q=1,2, \quad (\text{E24})$$

For POVM of the orthogonalized SPADE method given in Eq. E10,  $\left\{ \frac{1}{2} |\phi_{j,\pm}^{(l)}\rangle \langle \phi_{j,\pm}^{(l)}|, \frac{1}{2} |b_j^{(0)}\rangle \langle b_j^{(0)}| \right\}_{j=1,2,\dots,Q, l=0,1,2,\dots,\infty}$ , where  $|\phi_{j,\pm}^{(l)}\rangle = \frac{1}{\sqrt{2}} \left( |b_j^{(l)}\rangle \pm |b_j^{(l+1)}\rangle \right)$ , we can calculate

$$\begin{aligned} b_1^{(0)}(u) &= b_{1,0}(u), \\ b_2^{(0)}(u) &= p_1 b_{1,0}(u) + p_2 b_{2,0}(u), \quad p_1 = -\frac{e^{-(y_1-y_2)^2/8\sigma^2}}{\sqrt{1-e^{-(y_1-y_2)^2/4\sigma^2}}}, \quad p_2 = \frac{1}{\sqrt{1-e^{-(y_1-y_2)^2/4\sigma^2}}}, \\ b_1^{(1)}(u) &= p_3 b_{1,0}(u) + p_4 b_{2,0}(u) + p_5 b_{1,1}(u), \quad p_3 = \frac{\sqrt{4\sigma^2 + \frac{y_1 y_2}{2\sigma^2} \frac{(y_1-y_2)^2}{y_1^2+y_2^2} (y_1-y_2)}}{4 \left( -1 + e^{\frac{(y_1-y_2)^2}{4\sigma^2}} \right) \sigma^2 - (y_1-y_2)^2}, \\ p_4 &= \frac{e^{\frac{(y_1-y_2)^2}{8\sigma^2}} \sqrt{4\sigma^2 + \frac{y_1 y_2}{2\sigma^2} \frac{(y_1-y_2)^2}{y_1^2+y_2^2}} (-y_1+y_2)}{4 \left( -1 + e^{\frac{(y_1-y_2)^2}{4\sigma^2}} \right) \sigma^2 - (y_1-y_2)^2}, \quad p_5 = -\frac{2 \left( -1 + e^{\frac{(y_1-y_2)^2}{4\sigma^2}} \right) \sigma \sqrt{4\sigma^2 + \frac{y_1 y_2}{2\sigma^2} \frac{(y_1-y_2)^2}{y_1^2+y_2^2}}}{4 \left( -1 + e^{\frac{(y_1-y_2)^2}{4\sigma^2}} \right) \sigma^2 - (y_1-y_2)^2}. \end{aligned} \quad (\text{E25})$$

Higher-order basis states  $|b_q^{(l)}\rangle$  can be constructed similarly, though their explicit forms become too complex to present here.

There has been significant discussion regarding Hermite-Gaussian mode sorting [39–43], which enables the conversion of Hermite-Gaussian modes, with  $m = 0, 1, 2, \dots, \infty$  for a fixed  $q$ , into transverse momentum states. Note that when the PSF is Gaussian,  $b_{q,m}(u)$  in Eq. E24 corresponds to the Hermite-Gaussian mode. The transformation from Hermite-Gaussian modes to momentum states can be expressed as  $|m\rangle = F_q |b_{q,m}\rangle$ . Since the orthogonalized SPADE basis  $b_j^{(l)}(u)$  can be written as a linear combination of these Hermite-Gaussian modes  $b_{q,m}(u)$ , the mode converter  $F_q$ , allows for transforming the basis  $b_j^{(l)}(u)$  into simple transverse momentum states with some addition steps, thereby enabling complete measurement.

Fig. 15 illustrates the process of generating superpositions of nonorthogonal spatial modes  $|\psi_{a,b,c}\rangle$ , where each spatial mode  $|\psi_{a,b,c}\rangle$  can be created using the mode converter  $F_{a,b,c}^\dagger$  from a single photon in momentum states. Examples are shown for the cases of two and three distinct spatial modes, which can be easily extended to include additional modes. For the implementation of  $|\phi_{j,\pm}^{(l)}\rangle$ , we will need the spatial modes  $b_{q,m}(u)$  for  $q = 1, 2, \dots, Q$  when  $m \leq l$ , and  $q \leq j$  when  $m = l + 1$ . This procedure can be reversed to detect spatial modes as linear combinations of  $|b_{q,m}\rangle$ . Since both  $|\phi_{j,\pm}^{(l)}\rangle$  and  $|b_j^{(l)}\rangle$  can be expressed as linear combinations of  $|b_{q,m}\rangle$ , the orthogonalized SPADE method can be implemented using the Hermite-Gaussian mode converter with some additional steps.

The basis  $|b_j^{(l)}\rangle$  can be constructed differently from Eq. (E9) while preserving the key feature of the orthogonalized SPADE method—namely, ensuring that lower-order terms vanish in the probability distribution when estimating higher-order moments. This design enhances the performance of moment estimation. For instance, one could redefine the basis  $|\psi_k^{(m)}\rangle$  as a linear combination of  $|\psi_{j=1,2,\dots,Q}^{(m)}\rangle$  in the Eq. (E9) and then construct  $|b_j^{(l)}\rangle$  using the Gram-Schmidt procedure applied to the set of basis states  $|\psi_k^{(m)}\rangle_{k=1,2,\dots,Q; m=0,1,2,\dots}$ . This approach allows for the exploration of alternative constructions of  $|b_j^{(l)}\rangle$ . As the current construction is not necessarily the optimal choice for

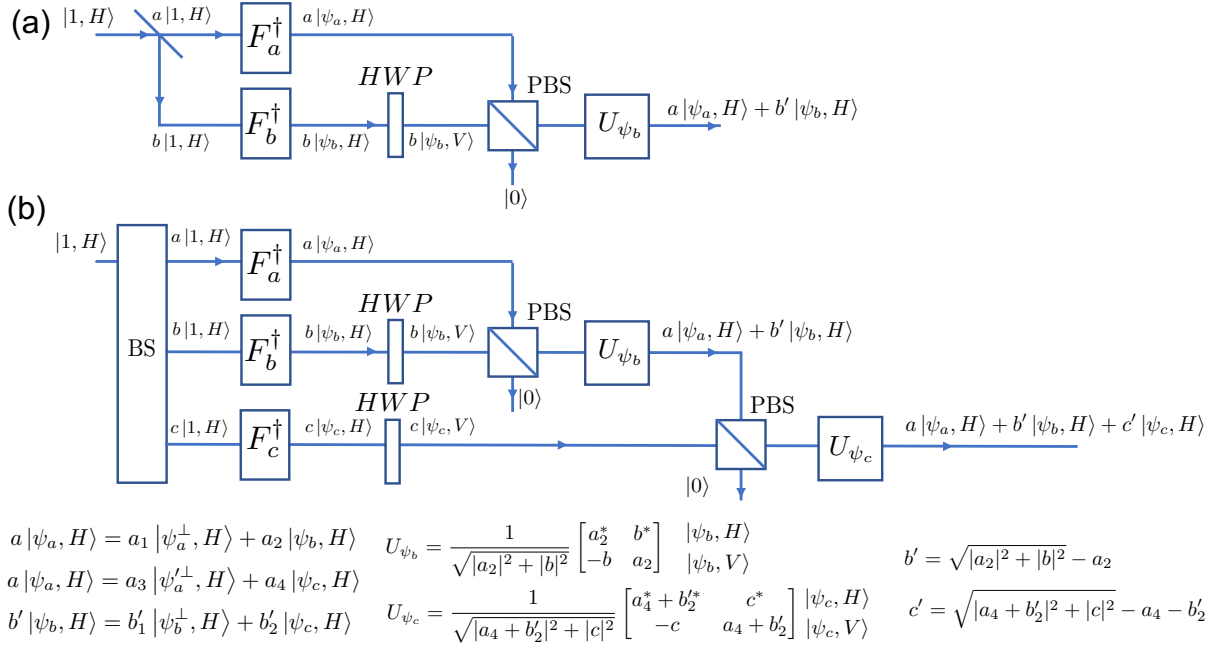


FIG. 15. Generation of a superposition of (a) two and (b) three nonorthogonal spatial modes using the mode converter  $F_{a,b,c}$ , which transforms the nonorthogonal spatial modes  $|\psi_{a,b,c}\rangle$  into transverse momentum states. The labels  $H$  and  $V$  denote the two polarizations. The setup includes polarizing beam splitter (PBS), beam splitter (BS), and half-wave plate (HWP). The operation  $U_{\psi_{b,c}}$  is applied to the two polarizations of the spatial mode  $|\psi_{b,c}\rangle$  to achieve the desired transformation.

experimental implementation, the flexibility in constructing the basis  $\{|b_j^{(l)}\rangle\}$  could potentially lead to simpler or more practical implementations of the orthogonalized SPADE method.

The implementation of the measurement must be sufficiently accurate to ensure that any deviations in the probability distribution due to imprecision remain smaller than the lowest-order terms of  $\alpha$  for each outcome. Consequently, the precision requirements for the measurement become increasingly stringent for higher-order moments.

## Appendix F: Details of numerical calculations

In our numerical calculations for the direct imaging case, we discretize the spatial coordinate for analysis, which is reasonable since, in practice, direct imaging involves pixels of finite size. Assuming the centroid of all compact sources or point sources is within the interval  $[-d/2, d/2]$ , we extend this range to  $[-d/2 - 5\sigma, d/2 + 5\sigma]$  for the PSF given by  $\psi(u) = \frac{\exp(-u^2/4\sigma^2)}{(2\pi\sigma^2)^{1/4}}$ . Because of the exponential decay of the PSF, this cutoff is expected to have a negligible impact on the results. We then select  $T_{\max}$  points at  $X_1, X_2, \dots, X_{T_{\max}}$  uniformly distributed across this interval, forming the set of POVMs  $\{M_i\}_{i=1,2,\dots,T_{\max}}$ , where each  $M_i = \int_{X_i - l/2}^{X_i + l/2} dx |x\rangle \langle x|$  and  $l = (d + 10\sigma)/T_{\max}$ . In the calculations presented in the main text, we use  $T_{\max} = 50$ , as further increasing  $T_{\max}$  does not show obvious difference. A plot illustrating the convergence of our calculations for different  $T_{\max}$  values confirms the stability of the results. Using the imaging of a single compact source as an example (Fig. 16), we show that varying  $T_{\max}$  does not affect the scaling behavior of  $\beta_k^2$  with  $\alpha$  or the stepwise increase of  $C_T$  with  $S$ . In theory,  $C_T$  should increase slightly with larger  $T_{\max}$  values due to the greater number of independent pixels; however, this effect is minimal in the numerical calculation. This is likely because, for compact source imaging, the information contained in the nearby pixel is largely similar.

For imaging of one compact source using the SPADE method [5], assume the PSF is again given by  $\psi(u) = \exp(-u^2/4\sigma^2)/(2\pi\sigma^2)^{1/4}$ . Using  $\rho = \sum_{m,n=0}^{\infty} x_{m+n} |\psi^{(m)}\rangle \langle \psi^{(n)}|$ , we will construct the orthonormal measurement basis  $\{|b_l\rangle\}_l$  such that

$$a_{ml} = \langle \psi^{(m)} | b_l \rangle = \begin{cases} = 0 & m \leq l - 1 \\ \neq 0 & m \geq l \end{cases} \quad (\text{F1})$$

$m \setminus l$	0	1	2	3	4
0	1	0	0	0	0
1	0	$\frac{1}{2}\alpha$	0	0	0
2	$-\frac{1}{8}\alpha^2$	0	$\frac{1}{4\sqrt{2}}\alpha^2$	0	0
3	0	$-\frac{1}{16}\alpha^3$	0	$\frac{1}{8\sqrt{6}}\alpha^3$	0
4	$\frac{1}{128}\alpha^4$	0	$-\frac{1}{32\sqrt{2}}\alpha^4$	0	$\frac{1}{32\sqrt{6}}\alpha^4$

TABLE I.  $a_{ml} = \langle \psi^{(m)} | b_l \rangle$  for the coefficient Eq. F1.

We can explicitly calculate the coefficients  $a_{ml}$ , the first few coefficients is shown in Table I as examples. If we define the measurement as in Eq. A5, the probability distribution of getting  $|b_0\rangle, |\phi_{k\pm}\rangle, k = 0, 1, 2, \dots$  is given by

$$\begin{aligned}
P_0 &= \frac{1}{2} \sum_{m,n=0}^{\infty} x_{m+n} a_{m,0}^* a_{n,0}, \\
P_{k,+} &= \frac{1}{4} \sum_{m,n=0}^{\infty} x_{m+n} (a_{m,k}^* a_{n,k} + a_{m,k+1}^* a_{n,k+1} + a_{m,k+1}^* a_{n,k} + a_{m,k}^* a_{n,k+1}), \\
P_{k,-} &= \frac{1}{4} \sum_{m,n=0}^{\infty} x_{m+n} (a_{m,k}^* a_{n,k} + a_{m,k+1}^* a_{n,k+1} - a_{m,k+1}^* a_{n,k} - a_{m,k}^* a_{n,k+1}).
\end{aligned} \tag{F2}$$

By comparing this concrete form of probability with the abstract form used earlier,  $P_0 = \sum_{m=0}^{\infty} c_m x_m \alpha^m$ ,  $P_{k,\pm} = \sum_{m \geq 2k} c_{km}^{\pm} x_m \alpha^m$  as in Eq. A7, we can determine the individual coefficients  $c_{nm}^{\pm}$ .

To perform the numerical calculations for single or multiple compact sources, we first define a specific form of prior

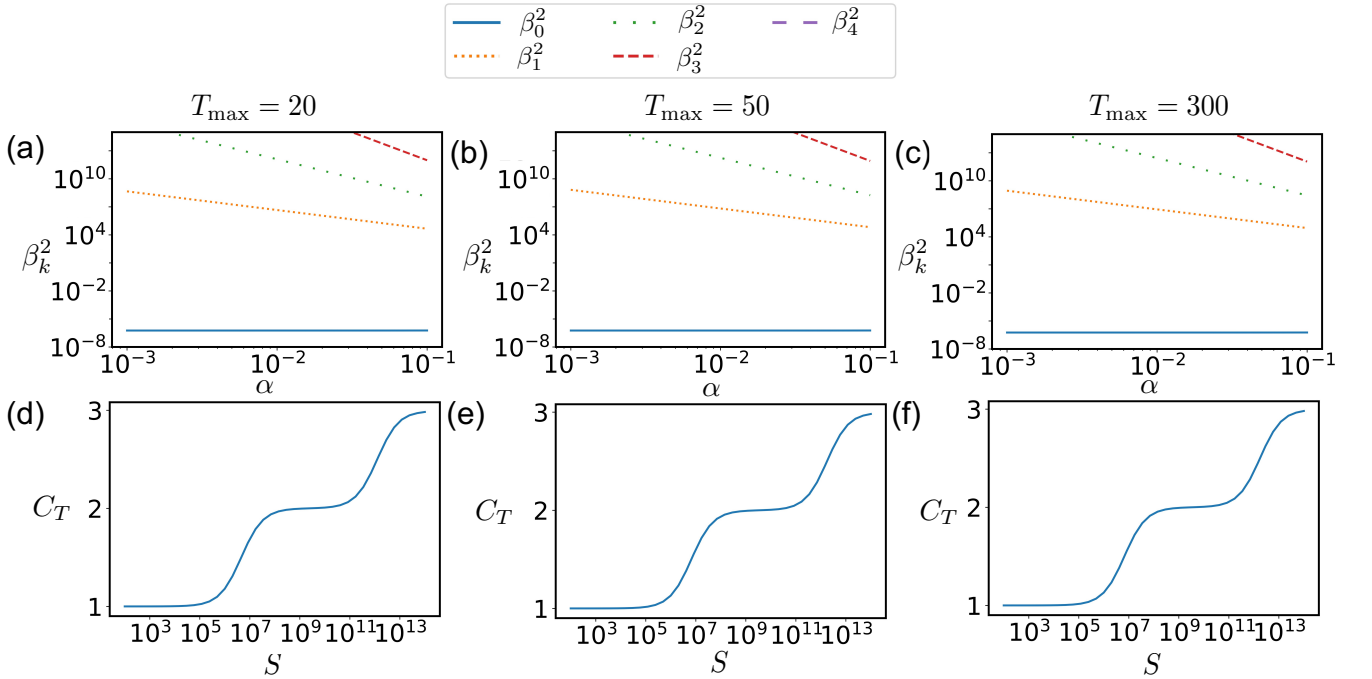


FIG. 16. Robustness of the numerical calculation for direct imaging with different discretization  $T_{\max}$ . The calculation is done for one compact source, and for (d)-(e) we choose  $\alpha = 10^{-2}$ . (Note in this subsection, we include  $\beta_0^2$  in the plot for  $\beta_k^2$  as a function of  $\alpha$ , which numerically appears slightly above zero due to finite numerical precision. This discrepancy could be minimized by increasing the calculation's precision. Additionally, we do not interpolate values of  $\beta_k^2$  above  $10^{15}$  with a straight line as in the main text; instead, we introduce a direct cutoff at  $10^{15}$ , beyond which numerical calculations lack sufficient precision.)

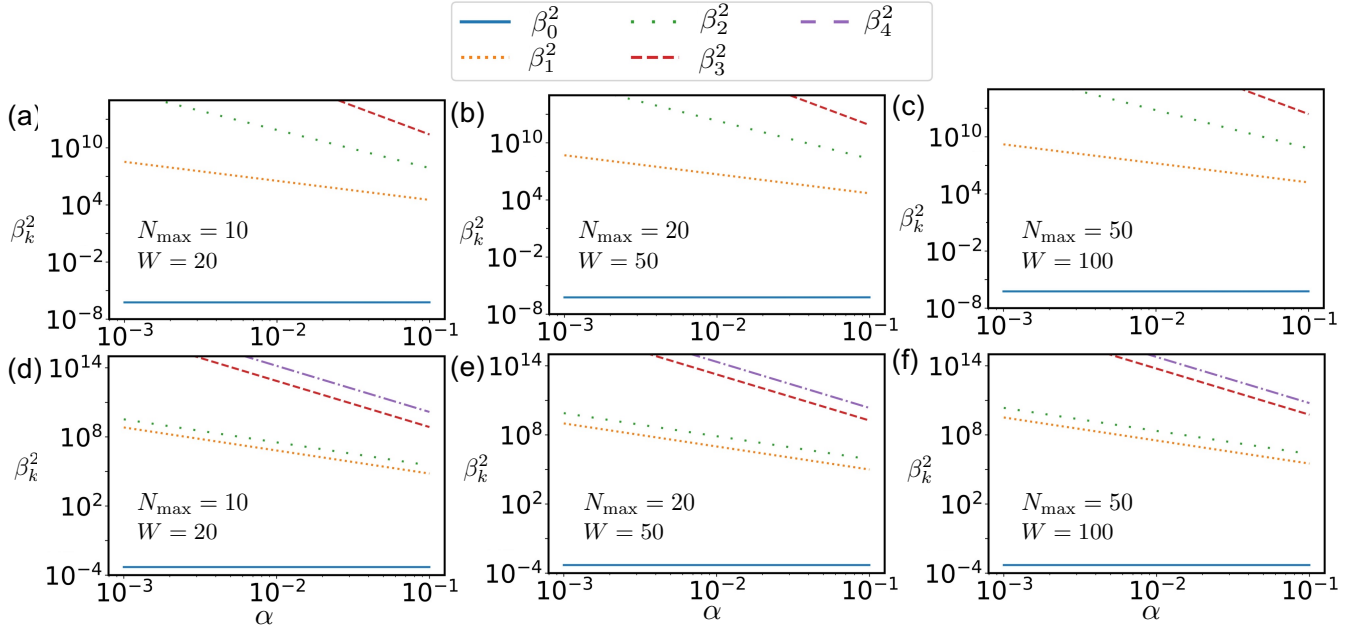


FIG. 17. The numerical calculation of  $\beta_k^2$  performed using various randomly generated sets of prior information, with different values for  $N_{\max}$  and  $W$ . We analyze the imaging of a single compact source using direct imaging and the SPADE method.  $\beta_4^2$  exceeds the cutoff at  $10^{15}$  for (a)-(c). In the main text, this line is interpolated using calculations for  $\alpha > 0.1$ .

knowledge  $p(\vec{x})$  for the input vectors  $\theta = \vec{x} = [x_0, x_1, x_2, \dots]$ , which we later use to compute  $g_{n_1 n_2} = \int d\vec{x} p(\vec{x}) x_{n_1} x_{n_2}$  and  $d_n = \int d\vec{x} p(\vec{x}) x_n$ , both essential for the calculations. To obtain the matrix elements  $d_n$  and  $g_{n_1 n_2}$ , we generate a series of one-dimensional images, each represented by a moment vector  $\vec{x}$  that fully characterizes it. This approach yields a set of  $W$  moment vectors, denoted  $\vec{x}(w)$ , where  $w$  indexes each generated vector. We then calculate  $d_n = \frac{1}{W} \sum_w x_n(w)$  and  $g_{n_1 n_2} = \frac{1}{W} \sum_w x_{n_1}(w) x_{n_2}(w)$ .

To generate these images, we divide the extent of each compact source, sized  $L_q$ , into  $N_{\max}$  segments and place a point source at the centroid of each segment, assigning it an intensity  $I_m$  uniformly distributed over  $[0,1]$ . As  $N_{\max}$  becomes sufficiently large, this configuration provides a high degree of freedom to model general compact sources. After randomly setting each point source's intensity, we normalize by replacing  $I_m$  with  $I_m / (\sum_m I_m)$ . Each point source has a defined coordinate, allowing us to compute the moment vector  $\vec{x}(w)$  for each generation. By repeating this process, we gather a full set of moment vectors  $\vec{x}(w)$ . In the calculations in the main text, we select  $N_{\max} = 20$  and  $W = 50$ , meaning each compact source is modeled by 20 evenly spaced point sources, and we generate 50 different sets of moments to compute  $d_n$  and  $g_{n_1 n_2}$ . For cases involving multiple compact sources with centroids separated by  $L$  and individual sizes  $L_q \ll L$ , we place the point sources only within each compact source of size  $L_q$ . The intensities are normalized so that the total intensity of all compact sources sums to one.

We emphasize that these randomly generated sources serve as a simple example to simulate prior knowledge and to demonstrate our approach. However, the discussion in the main text applies to any general prior information about the moments  $\vec{x}$ . It is important to note that a set of images is needed to generate the matrices  $g_{n_1 n_2}$  and  $d_n$ ; using only one image would make  $g_{n_1 n_2}$  a rank-one matrix, implying that the moment of the image is already known, hence no additional information can be obtained through measurement.

We examine the impact of varying  $M$  and  $W$  on both the scaling of  $\beta_k^2$ , shown in Fig. 17, and the  $C_T$  vs.  $S$  plot, shown in Fig. 18. As we increase  $N_{\max}$  and  $W$ , the scaling of  $\beta_k^2$  with  $\alpha$  and the stepwise increase of  $C_T$  as a function of  $S$  remains the same. However, a careful reader may observe that as  $N_{\max}$  and  $W$  grow,  $\beta_k^2$  exhibit a slight increase, as can be seen by comparing Fig. 17(a) with Fig. 17(c). This trend is also evident in Fig. 18(c1) and Fig. 18(c3), where the threshold for each stepwise increment rises. This effect occurs because the prior knowledge influences the prefactor of the eigenvalues  $\beta_k^2$ . Numerically, we observe the prefactors of  $\beta_k^2$  tend to increase as the eigenvalues of  $g_{n_1 n_2}$  decrease. If  $g_{n_1 n_2}$  is full rank, the prior information is not expected to influence the scaling of  $\beta_k^2$ .

The method described above generates a unique random prior knowledge for each execution, resulting in a different set of  $g$  and  $d$  for every run. In all the discussions in this work, the plots are generated using a single instance of randomly generated prior knowledge. To verify that our method works universally for any prior information, we run the code multiple times and observe that each instance of prior knowledge produces a similar scaling of  $\beta_k^2$  with  $\alpha$ , as

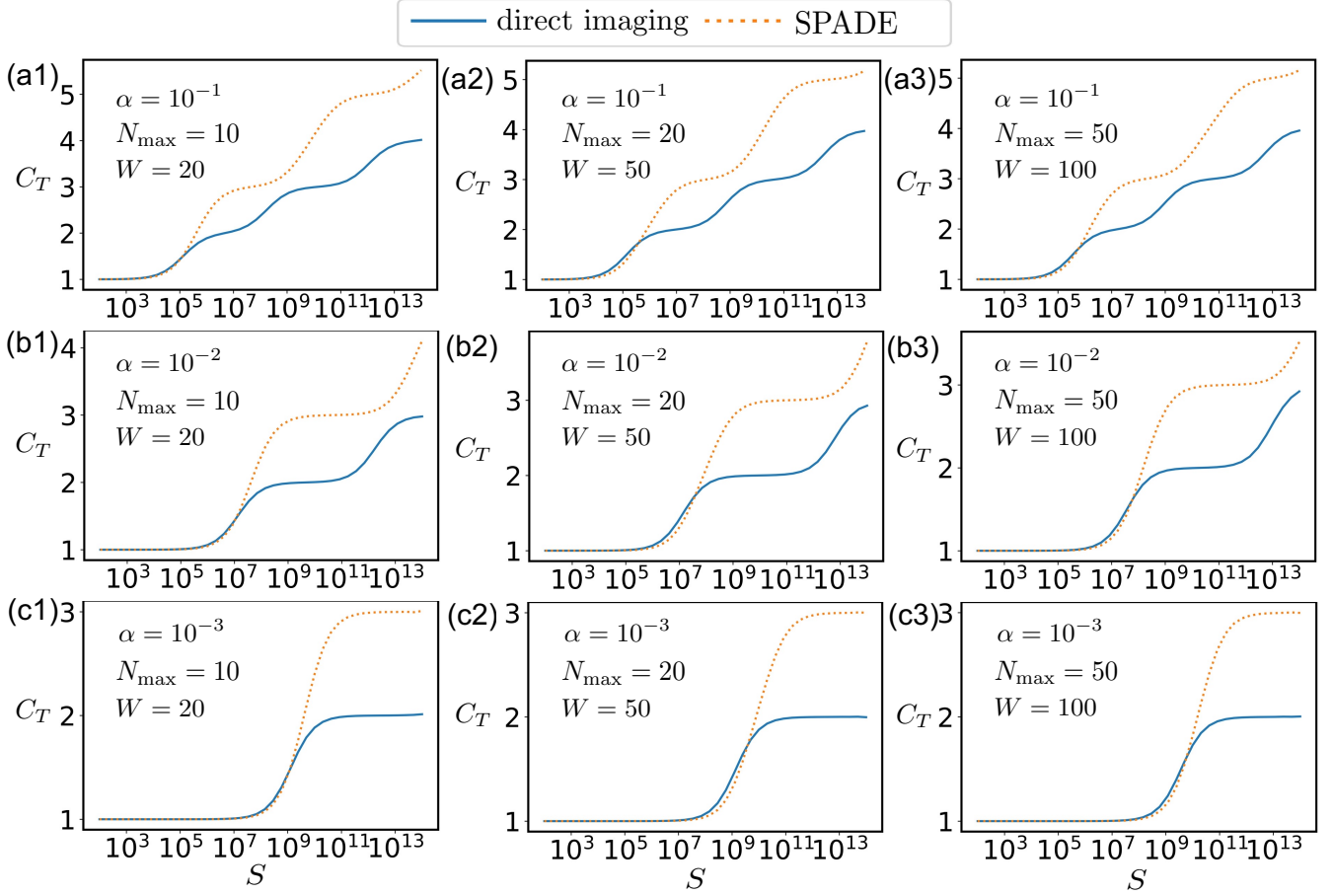


FIG. 18. The numerical calculation of REC  $C_T$  as a function of  $S$  performed using various randomly generated sets of prior information, with different values for  $N_{\max}$  and  $W$ . We analyze the imaging of a single compact source using direct imaging and the SPADE method.

expected. Consequently,  $C_T$  consistently displays a stepwise increase as a function of  $S$ . In Fig. 19, we present results for three randomly generated instances of prior knowledge using this method. In these three instances,  $g$  and  $d$  differ due to the difference of prior information. While the eigenvalues and  $C_T$  vary with the prior knowledge, the scaling behavior of  $\beta_k^2$  remains consistent, ensuring the stepwise increase of  $C_T$  is always observed.

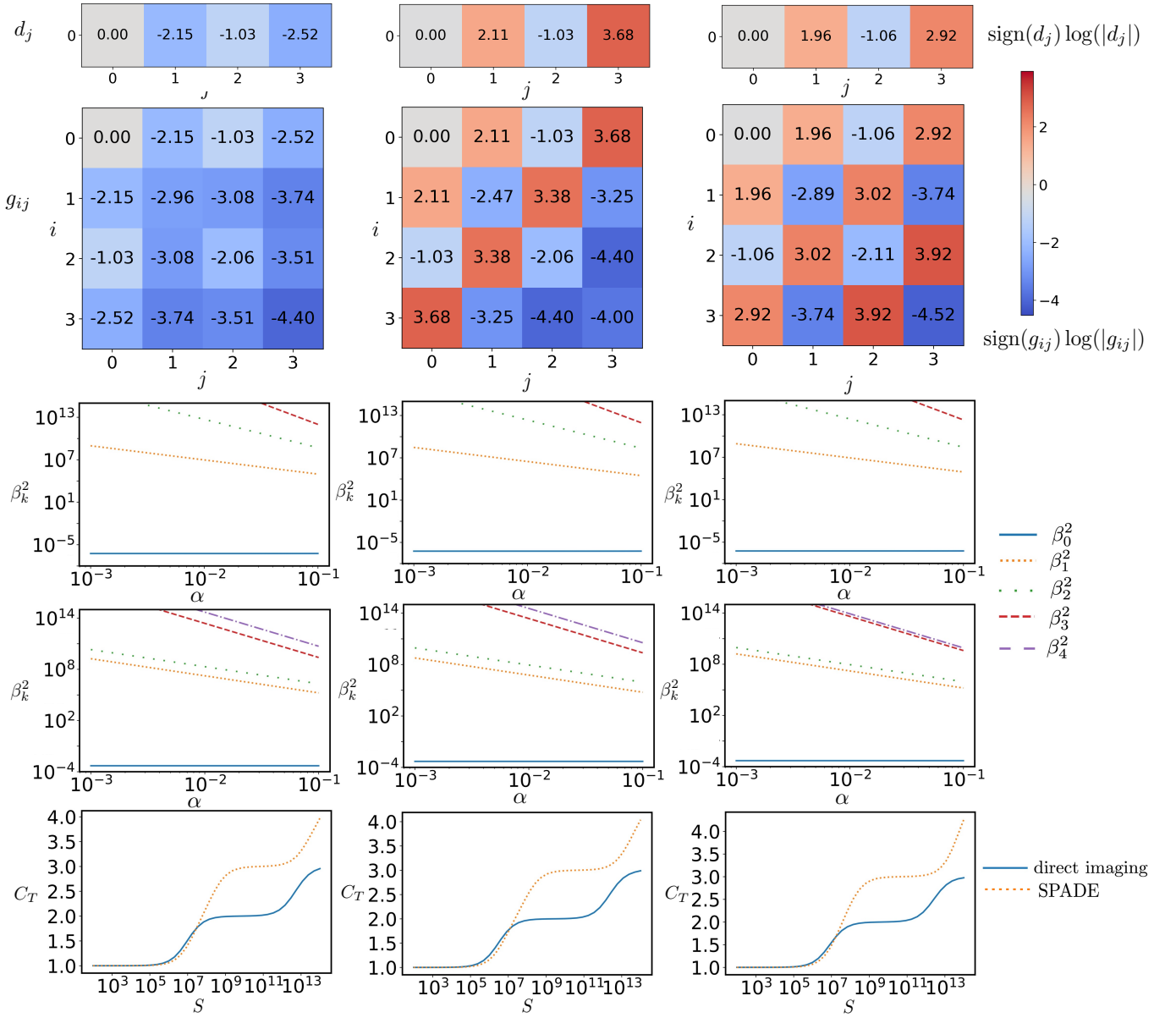


FIG. 19. The numerical calculation of REC  $C_T$  as a function of  $S$  when  $\alpha = 10^{-2}$  and  $\beta_k^2$  as a function of  $\alpha$ . The calculation is performed using three different prior information randomly generated when  $N_{\max} = 10$ ,  $W = 20$ . The first few elements of  $d, g$  for these three different prior information are given. We analyze the imaging of a single compact source using direct imaging and the SPADE method.